(8) : 554-555, 2003.
2) 紀ノ岡正博：移植を前提としたヒト培養組織に生産に関する生物化学工学的研究．生物工学会誌 82(3) : 95-100, 2004.
3) 紀ノ岡正博，田谷正仁：組織培養における細胞評価，化学工学会関東支部編．最近の化学工学56－先端医療における化学工学．化学工業社：東京，79-97 : 2004.
4) Kino-oka M, Prenosil J E : Development of On-Line Monitoring System of Human Keratinocyte Growth by Image Analysis and Its Application to Bioreactor Culture. Biotechnol Bioeng 67(2) : 234-239, 2000.
5) Kino-oka M, Agatahama Y, Hata N, Taya M : Evaluation of Growth Potential of Human Epithelial Cells by Motion Analysis of Pairwise Rotation under Glucose-Limited Condition. Biochem Eng J 19(2) : 155-158, 2004.
6) Umegaki R, Murai K, Kino-oka M, Taya M : Correlation of Cellular Life Span with Growth Parameters Observed in Successive Cultures of Human Keratinocytes. J Biosci Bioeng 94(3) : 231-236, 2002.
7) Hata N, Hirai H, Kino-oka M, Taya M : Comprehension of Attachment and Multiplication Properties by Observing Individual Cell Behaviors in Anchorage-Dependent Culture. Biochem Eng J 20(2-3) : 197-202.2004.
8) Hata N, Murai K, Kino-oka M, Taya M : Acute Responses of Cell Individuals Observed after Calcium Administration in Human Keratinocyte Culture. Biochem Eng J 18(2) : 155-158, 2004.
9) Kino-oka M, Agatahama Y, Haga Y, Inoie M, Taya M : Long-term Subcultures of Human Keratinocytes under an Anoxic Condition. J Biosci Bioeng 100(1) : 119-122, 2005.
10) Hata N, Agatahama Y, Kino-oka M, Taya M : Relations between Individual Cellular Motions and Proliferative Potentials in Successive Cultures of Human Keratinocytes. Cytotechnology in press, 2005.

JOURNAL OF BIOSCIENCE AND BIOENGINEERING
Vol. 104, No. 5, 428–431. 2007
DOI: 10.1263/jbb.104.428

Synergistic Effect of D-Glucose and Epidermal Growth Factor Display on Dynamic Behaviors of Human Epithelial Cells

Mee-Hae Kim,[1] Masahiro Kino-oka,[2] Masaya Kawase,[3]
Kiyohito Yagi,[4] and Masahito Taya[1,2]*

Department of Biotechnology, Graduate School of Engineering, Osaka University, 2-1 Yamada-oka, Suita, Osaka 565-0871, Japan,[1] Division of Chemical Engineering, Graduate School of Engineering Science, Osaka University, 1-3 Machikaneyama-cho, Toyonaka, Osaka 560-8531, Japan,[2] Faculty of Pharmaceutical Sciences, Osaka-ohtani University, 3-11-1 Nishiki-ori, Tondabayashi, Osaka 584-8540, Japan,[3] and Graduate School of Pharmaceutical Sciences, Osaka University, 1-6 Yamada-oka, Suita, Osaka 565-0871, Japan[4]

Received 14 May 2007/Accepted 9 August 2007

We investigated the synergistic effect of D-glucose and epidermal growth factor (EGF) display on the dynamic cellular behaviors of morphology and migration in a culture of human epithelial cells. The time-lapse observation revealed that the cells on the D-glucose/EGF-displayed substrate were endowed with enhanced migration, accompanied with periodic changes in morphology between round and stretched shapes. Immunofluorescence staining of phosphotyrosine PY20 and vinculin was conducted to determine the intracellular localization of phosphorylated tyrosine expression and focal contact formation, respectively. On the substrate displaying D-glucose and EGF, the cells exhibited increases in the levels of the expression of phosphorylated tyrosine and the formation of focal contacts not only at the cellular periphery but also in the cell body. These findings supported the consideration that the displayed D-glucose causes the cells to be in close contact with the surface via grasping glucose transporters on the cytoplasmic membrane.

[**Key words:** human epithelial cells, glucose/epidermal growth factor co-display, migration rate, cell roundness]

Growth factors are generally accepted as essential mediators affecting cell migration, proliferation and differentiation during *in vitro* culture. The regulation of cellular responses in terms of magnitude and duration by growth-factor-derived stimulation is one of the most critical issues that need to be investigated. In many studies, it has been reported that growth factors can be dosed in a nonendocytosible and nondiffusable form to induce signal transduction via interactions between growth factors and their receptors on the cytoplasmic membrane (1), leading to the idea that the immobilization of growth factors on solid substrates is one of promising methods.

Ito and co-workers (2–4) demonstrated that an immobilized form of epidermal growth factor (EGF) is sustainably active for the p38 mitogen-activated protein kinase (MAPK) and that MAPK activation induced by its soluble form deteriorates rapidly with elapsed time in cultures of anchorage-dependent cells. Moreover, they stated that the immobilized EGF enhanced the cell division to a greater extent than EGF solublized in medium, providing evidence that an immobilized growth factor can induce an altered signal transduction. To realize the effective stimulation intensified through respective interactions in signal-transduction systems, the coimmobilization of growth factors and tethering molecules has been proposed, leading to surface designs to enhance the cell anchoring accompanied with the promotion of focal contact (5–7).

In our previous study (8), a D-glucose-displayed substrate was designed to enhance cell anchoring, which was mediated by not only integrin but also a glucose transporter on the cytoplasmic membrane in a culture of human epithelial cells. In the present study, we propose an extended design of the substrate targeting EGF stimulation through the improvement of cell anchoring and migration induced by the concurrent display of D-glucose and EGF. The dynamic behaviors of cell morphology and migration were investigated to evaluate the extent of EGF stimulation on the prepared substrate.

A conventional plastic surface of a 25-cm^2 T-flask (Nunclon Delta Flask; Nalge Nunc, Roskilde, Denmark) was used as a starter material for displaying glucose and EGF. A template with a dendron structure on the surface was produced according to a method reported previously (8). In brief, an aqueous solution of 50 μmol/ml potassium *tert*-butoxide was poured into the flask to generate hydroxide groups on the surface. After washing with sterilized water, a glutaraldehyde solution (360 μmol/ml) was added, and allowed to stand for 1 h, followed by washing with a large amount of sterile water. To generate amino groups on the dendron structure, the flask was treated with a 360 μmol/ml tris(2-aminoethyl) amine solution and then rinsed with sterile water.

* Corresponding author. e-mail: taya@cheng.es.osaka-u.ac.jp
phone: +81-(0)6-6850-6251 fax: +81-(0)6-6850-6254

TABLE 1. Culture conditions examined in this study

Condition no.	Substrate	Total amount of EGF (ng/flask)	EGF concn in medium (ng/ml)	EGF density on substrate (ng/cm^2)
1	Plain	3.58×10^3	358.1	0
2	D-Glucose/EGF	3.58×10^3	0.1	143 (0.53)
3	L-Glucose/EGF	3.58×10^3	0.1	143 (0.53)
4	Plain	1.0	0.1	0

The values in the parentheses indicate the standard deviation (n=3).

By means of a cross-linking reaction with 360 μmol/ml glutaraldehyde for 1 h, aldehyde groups were introduced onto the dendron structure. To display glucose and EGF (Sigma-Aldrich, St. Louis, MO, USA) on the terminal ligands, the substrate prepared as mentioned above was immersed in phosphate-buffered saline (PBS) containing ethylenediamine (8 mmol/ml) and EGF (10 μg/ml) for 6 h at room temperature. After washing, a D- or L-glucose solution (0.5 μg/ml) was added to and left in each flask for 2 h. A sodium borohydride solution (0.5 μmol/ml) was poured into the flask, and was left to sit for 2 h. Until use in experiments, each flask with the prepared substrate was kept at 4°C. Here, the amount of EGF displayed on the substrate was determined directly by bicinchoninic acid protein assay (9, 10).

Human epithelial cells (hTERT-HME1; Clontec Laboratories, San Diego, CA, USA) were incubated in 25-cm^2 T-flasks with plain and modified surfaces, at 37°C under a 5% CO_2 atmosphere. The cells were cultivated in serum-free medium (HuMedia-KG2; Kurabo Industries, Osaka), which contained 0.1 ng/ml EGF as a growth stimulator in the liquid phase under a conventional condition. The initial concentration of viable cells, determined by trypan blue exclusion, was set at $X_0=5.0\times10^3$ cells/cm^2. The main culture conditions examined are shown in Table 1.

The time-lapse image capturing was carried out to investigate dynamic cell behaviors using an observation tool described elsewhere (11). The images were captured at 20 min intervals for 6 positions on the bottom surface of the flask. For cell tracing, a rectangular coordinate system was placed on the captured images, and the origin of the coordinate system was defined as the position at which the cell of interest was located at the onset of observation. The sequence of positioning for each cell was initiated within 1 h of seeding. In addition, cell migration rate, R_m, was estimated from the distance of cells moved in the 20-min observation. The morphological variation was also investigated in terms of cell roundness, R_c, which was calculated by

$$R_c=2(\pi A_c)^{1/2}/l_c$$

Here, A_c and l_c are the projected area and peripheral length of each cell, respectively. The mean cell migration rate, $\bar{R}_m$, and cell roundness, $\bar{R}_c$, were obtained separately from populational averages from a set of data on 10–15 cells, which was recorded in advance as time-mean values evaluated until the first cell division after starting the observation.

For immunofluorescence staining, the cultured cells were washed three times with PBS and fixed with 4% paraformaldehyde in PBS for 10 min at room temperature. The cells were then rinsed with PBS and permeabilized by incubation for 3 min in 0.5% Triton X-100. After washing with PBS, nonspecific binding sites on the cells were masked by treating the cells with Block Ace (Dainippon Sumitomo Pharma, Osaka) for 1 h. The cells were then kept at 4°C overnight in 0.05% Tween 20/PBS containing anti-rabbit vinculin (Sigma-Aldrich) or anti-mouse phosphotyrosine antibody PY20 (BD Transduction Laboratory, San Jose, CA, USA) at an appropriate dilution ration for the antibody. After being washed with PBS and rinsed with Tris-buffered saline (DakoCytomation, Carpinteria, CA, USA), the cells were subjected to immunolabeling with Alexa Fluor 488 goat anti-mouse or Alexa Fluor 568 goat anti-rabbit IgG (Molecular Probes, Eugene, OR, USA). The sample was then thoroughly washed and mounted on a specimen slide, followed by fluorescence observation using a confocal laser scanning microscope (model FV-300; Olympus, Osaka).

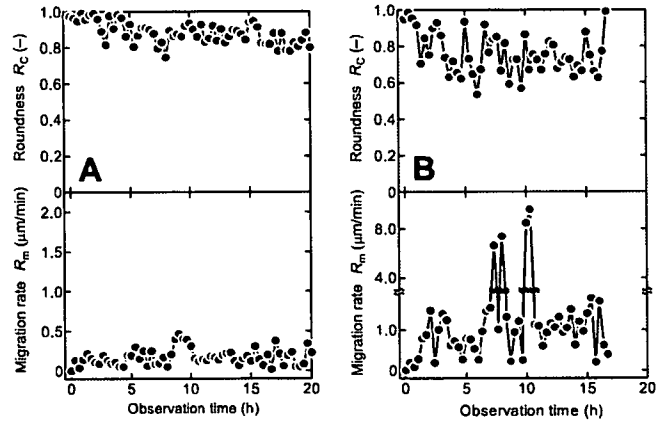

FIG. 1. Dynamic cell behaviors in terms of migration rate and roundness of representative cells cultured under conditions 1 (A) and 2 (B) shown in Table 1.

To characterize the dynamic behaviors of the epithelial cells stimulated by soluble or insoluble EGF, time-lapse observation was started within 1 h after seeding. Figure 1 shows the time profiles of R_m and R_c under conditions 1 and 2 (Table 1). In the control culture on the plain surface with EGF stimulation in the liquid phase (condition 1), it was found that the ranges of R_m and R_c were approximately 0.23 μm/min and 0.88 on average, respectively. In the case of culture on the D-glucose/EGF-displayed substrate (condition 2), the enhancement of cell migration rate occurred, resulting in a maximum R_m of 9.6 μm/min, which was 20-fold that in the culture under condition 1. Under condition 2, the fluctuation in cell morphology was also appreciable with periodic alternation between low and high R_c values. The dynamic change in the morphology of the cells observed on the D-glucose/EGF-displayed substrate is visually presented in Fig. 2. The migration for 2 h was accompanied with undulatory movements of cells (Fig. 2, arrow A). In addition, a remarkable change in shape between the extreme extension and contraction of the cells was observed occasionally (Fig. 2, arrow B), and a part of the tail at cellular rear was severed owing to active migration (Fig. 2, arrow B'). These results suggest that the partial anchoring mediated by glucose transporters (GLUTs) causes the securing of the tail during the migration, and that the high migration rate on the D-glucose/EGF-displayed substrate leads to the delay of retraction at the cellular rear, thereby inducing the temporal cell extension.

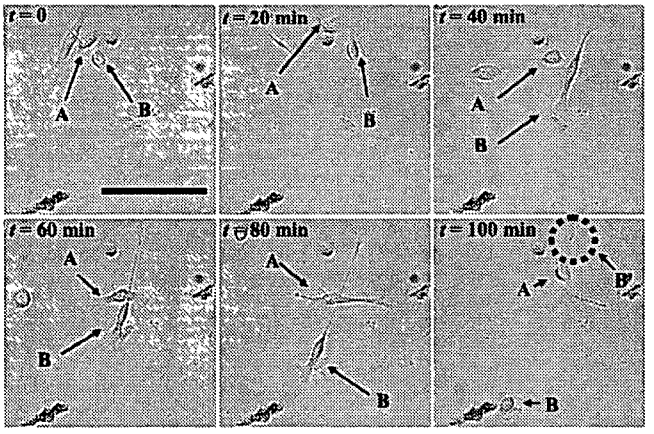

FIG. 2. Demonstration of dynamic cell morphology during migration on D-glucose/EGF displayed substrate (condition 2 shown in Table 1). The cell marked by arrow A was the same cell examined under condition 2 in Fig. 1. The cell marked by arrow B suffered extreme elongation severing its tail (marked by arrow B'), owing to migration. The scale bar indicates 100 μm.

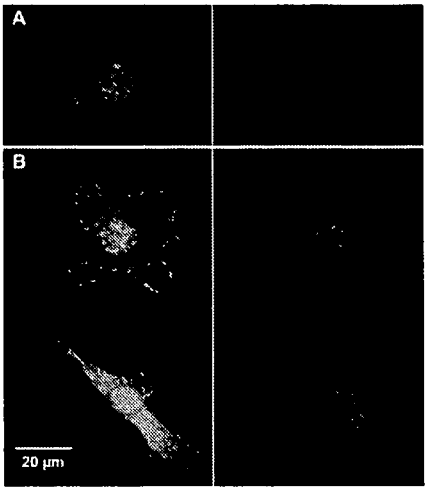

FIG. 3. Immunostaining of phosphotyrosine PY20 (green) and vinculin (red) in cells cultured for 24 h under conditions 1 (A) and 2 (B) shown in Table 1.

To confirm the activation of EGF receptors, fluorescence microscopy for phosphotyrosine PY20 and vinculin was conducted using the cells obtained at 24 h of culture time. As shown in Fig. 3, the distinct PY20 spots in the cells on the D-glucose/EGF-displayed substrate (condition 2) can be observed not only at the cell periphery but also in the cell body, and they overlap with vinculin spots, suggesting that the phosphorylation of EGF receptors occurred with generating focal contacts. However, no distinct spots of PY20 appeared in the cells obtained from the control culture (condition 1).

The values of $\bar{R}_m$ and $\bar{R}_c$ were estimated to compare the extent of EGF stimulation under the different conditions. As shown in Fig. 4, the cells on the L-glucose/EGF-displayed substrate (condition 3) were enhanced to some extent in terms of migration with an $\bar{R}_m$ of 0.56 μm/min, as compared with the $\bar{R}_m$ under condition 1, the latter being comparable to that in the conventional culture condition (condition 4). As expected, a significant enhancement of $\bar{R}_m$ on the D-glucose/EGF-displayed substrate (condition 2) was achieved, yielding an $\bar{R}_m$ of 1.19 μm/min, which is 2.1 and 4.1-fold in the cases of conditions 3 and 4, respectively. To confirm the synergistic effect of D-glucose and EGF display on the migration, we carried out a culture on a substrate displaying D-glucose alone using EGF-enriched medium (358.1 ng-EGF/ml). Under this culture condition, it was found that the stimulation of cell migration did not occur, giving a low value of $\bar{R}_m$, comparable to that in the case of condition 1 (data not shown). Concerning the morphology of cells, almost no variation in $\bar{R}_c$ was observed under conditions 1, 3 and 4, giving an $\bar{R}_c$ of approximately 0.9, whereas the lowest $\bar{R}_c$ was attained under condition 2 ($\bar{R}_c = 0.75$), being in agreement with the finding that the D-glucose and EGF display caused the elongation of cells, owing to the undulatory movement (Fig. 2).

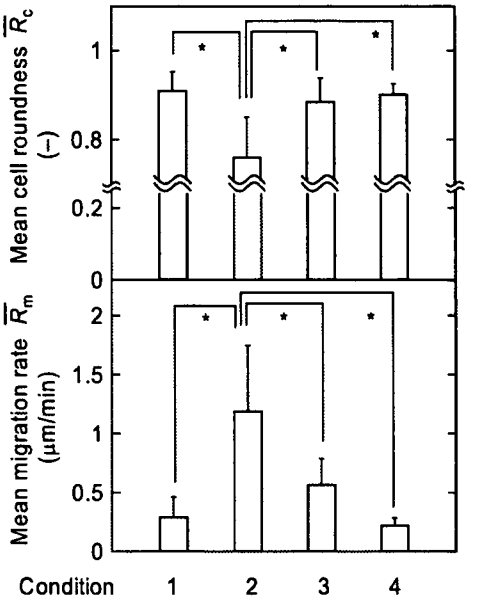

FIG. 4. Mean values of migration rate and roundness of cells cultured under conditions 1–4 shown in Table 1. The vertical bars indicate the standard deviation (n=10–15). The asterisks indicate the difference in statistical significance (p<0.01) between the data under conditions 2 and 1, 3 or 4, confirmed on the basis of analysis of variance (ANOVA).

For successful outcomes in tissue engineering, it is necessary to understand how cells are stimulated by biologically active factors targeting receptors on the cytoplasmic membrane, which can be categorized mainly into three groups, namely, autocrine, paracrine and juxtacrine (12). The autocrine and paracrine are accompanied with signaling mechanisms involving receptor activation with a soluble form of stimulator, and the juxtacrine is derived from an insoluble form on extracellular matrixes (13–15). It has been reported that juxtacrine stimulation was mimicked by immobilizing growth factors on a solid substrate. Kuhl and Griffth-Cima reported that EGF tethered on an aminosilane-modified glass substrate retained its biological activity in terms of eliciting DNA synthesis, preserving round cell shape and enhancing the cell growth of primary rat hepatocytes, in spite of the relatively low stimulation activity of EGF in a soluble state

(13). By examining the phosphorylation of signal proteins such as MAPK, they pointed out that the activation of signal transduction proteins via stimulation from a solid substrate lasted for a longer period, compared with that in the case of a soluble form, because the immobilization caused the sustained activity of signaling owing to a continuous expression of EGF receptors by preventing EGF from being taken into the cells. These results support the view that immobilized EGF can regulate cell functions without internalized latency, and thereby enhance intracellular signaling (3, 4).

The coimmobilization of growth factors and tethering molecules to solid substrates provides an intelligent design that elicits spatiotemporal responses and mimics juxtacrine signaling (13, 14). This coimmobilization strategy is expected to have a synergy effect on cellular behaviors owing to stimulatory increases in frequency and intensity. As examined in this study, the frequency of interaction between EGF on substrate and its receptor on the cytoplasmic membrane increases with an increase in the number of focal contacts, which occur via integrin-mediated anchoring, and the intensity of signaling from the activated EGF receptor is enhanced with the outside-in signaling of integrin. GLUTs exhibit a sharp specificity for high binding affinity against D-glucose, while having an extremely low binding affinity against L-glucose (15). Our previous study demonstrated that D-glucose display permitted cells to be in close contact with a solid surface through the grasping of GLUTs on the cytoplasmic membrane (8). In addition, this GLUT-mediated anchoring caused an undulatory movement in cells following temporal stretching with repetition between low and high R_c values. As discussed above, displayed D-glucose molecules yield a larger number of contact points between the cell and substrate, resulting in an enhanced formation of focal contacts. Considering the overlapping spots of PY20 and vinculin (Fig. 3), D-glucose display is considered to permit the cells to be in close contact with the substrate via the grasping of GLUTs on the cytoplasmic membrane, owing to the increase in the number of focal contacts, which can induce the up-regulation of EGF receptor signaling. Thus, the coimmobilization of EGF and D-glucose offers a substrate that allows the EGF receptor to be further activated in association with cellular binding mediated by GLUTs and integrin.

In conclusion, in this work, we suggest that GLUT-mediated anchoring can offer a synergistic enhancement of the cell signaling by the concurrent display of D-glucose and EGF molecules, because D-glucose display induces the advantage to promote the formation of the focal contacts, leading to an enhanced stimulation. The display of D-glucose together with growth factors mimics juxtacrine stimulation and can be used for the reconstruction of cultured tissues.

This study was conducted as part of the programs "Center for integrated cell and tissue regulation" for the 21st COE. This work also received financial supports in part by a Grant-in-Aid for Scientific Research (no. 17360398) from the Ministry of Education, Culture, Sports, Science and Technology and by a grant for Research on the Human Genome, Tissue Engineering and Food Biotechnology from the Ministry of Health, Labour, and Welfare, Japan.

REFERENCES

1. **Roy, S. and Herbst, M. D.:** Review of epidermal growth factor receptor biology. Int. J. Radiat. Oncol. Biol. Phys., **59**, S21–S26 (2004).
2. **Chen, G., Ito, Y., and Imanishi, Y.:** Photo-immobilization of epidermal growth factor enhances its mitogenic effect by artificial juxtacrine signaling. Biochim. Biophys. Acta, **1358**, 200–207 (1997).
3. **Ito, Y., Li, J.-S., Takahashi, T., Imanishi, Y., Okabayashi, Y., Kido, Y., and Kasuga, M.:** Enhancement of the mitogenic effect by artificial juxtacrine stimulation using immobilized EGF. J. Biochem., **121**, 514–520 (1997).
4. **Ito, Y., Liu, S. Q., and Imanishi, Y.:** Enhancement of cell growth on growth factor-immobilized polymer film. Biomaterials, **12**, 449–453 (1991).
5. **Vella, F., Thielens, N. M., Bersch, B., Arlaud, G. J., and Farchet, P.:** A recombinant chimeric epidermal growth factor-like module with high binding affinity for integrins. J. Biol. Chem., **278**, 19834–19843 (2003).
6. **Bos, G. W., Scharenborg, N. M., Poot, A. A., Engbers, G. H. M., Beugling, T., van Aken, W. G., and Feijen, J.:** Proliferation of endothelial cells on surface-immobilized albumin-heparin conjugate loaded with basic fibroblast growth factor. J. Biomed. Mater. Res., **44**, 330–340 (1998).
7. **Hayashi, M., Tomita, M., and Yoshizato, K.:** Production of EGF-collagen chimeric protein which shows the mitogenic activity. Biochim. Biophys. Acta, **528**, 187–195 (2001).
8. **Kino-oka, M., Morinaga, Y., Kim, M.-H., Isoda, K., Kawase, M., Yagi, K., and Taya, M.:** Morphological regulation of rabbit chondrocytes on glucose-displayed surface. Biomaterials, **28**, 1680–1688 (2007).
9. **Smith, P. K., Krohn, R. I., Hermanson, G. T., Mallia, A. K., Gartner, F. H., Provenzano, M. D., Fujimoto, E. K., Goeke, N. M., Olson, B. J., and Klenk, D. C.:** Measurement of protein using bicinchoninic acid. Anal. Biochem., **150**, 76–85 (1985).
10. **Kato, K., Sato, H., and Iwata, H.:** Immobilization of histidin-tagged recombinant proteins onto micropatterned surfaces for cell-based functional assays. Langmuir, **21**, 7071–7075 (2005).
11. **Kino-oka, M., Agatahama, Y., Hata, N., and Taya, M.:** Evaluation of growth potential of human epithelial cells by motion analysis of pairwise rotation under glucose-limited condition. Biochem. Eng. J., **19**, 109–117 (2004).
12. **Singh, A. B. and Harris, R. C.:** Autocrine, paracrine and juxtacrine signaling by EGFR ligands. Cell. Signal, **17**, 1183–1193 (2005).
13. **Kuhl, P. R. and Griffith-Cima, L. G.:** Tethered epidermal growth factor as a paradigm for growth factor-induced stimulation from the solid phase. Nat. Med., **2**, 1022–1027 (1996).
14. **Dong, J., Opresko, L. K., Chrisler, W., Orr, G., Quesenberry, R. D., Lauffenburger, D. A., and Wiley, H. S.:** The membrane-anchoring domain of epidermal growth factor receptor ligands dictate their ability to operate in juxtacrine mode. Mol. Biol. Cell, **16**, 2984–2998 (2005).
15. **Spravchikov, N., Sizyakov, G., Gartsbein, M., Accili, D., Tennenbaum, T., and Wertheimer, E.:** Glucose effects on skin keratinocytes; implications for diabetes skin complications. Diabetes, **50**, 1627–1635 (2001).

Journal of Chemical Engineering of Japan, Vol. 40, No. 1, pp. 51–58, 2007 **Research Paper**

Incorporation of Capillary-Like Structures into Dermal Cell Sheets Constructed by Magnetic Force-Based Tissue Engineering

Kosuke INO[1,2], Akira ITO[3], Hirohito KUMAZAWA[1], Hideaki KAGAMI[4], Minoru UEDA[5] and Hiroyuki HONDA[1]

[1]*Department of Biotechnology, School of Engineering, Nagoya University, Furo-cho, Chikusa-ku, Nagoya-shi, Aichi 464-8603, Japan*

[2]*Reseach Fellow of the Japan Society for the Promotion of Science (JSPS Research Fellow), Japan*

[3]*Department of Chemical Engineering, Faculty of Engineering, Kyushu University, 744, Motooka, Nishi-ku, Fukuoka-shi, Fukuoka 819-0395, Japan*

[4]*Department of Tissue Engineering, School of Medicine, Nagoya University, 65, Turumai-cho, Showa-ku, Nagoya-shi, Aichi 466-8550, Japan*

[5]*Department of Oral and Maxillofacial Surgery, School of Medicine, Nagoya University, 65, Turumai-cho, Showa-ku,, Nagoya-shi, Aichi 466-8550, Japan*

Keywords: Magnetite Nanoparticle, Liposome, Angiogenesis, Co-culture, Dermis

One of the major challenges in tissue engineering remains the construction of vascularized 3D transplants *in vitro*. We recently proposed novel technologies, termed "magnetic force-based tissue engineering" (Mag-TE), to establish three-dimensional (3D) tissues without using scaffolds. Magnetite cationic liposomes (MCLs), which contain 10-nm magnetite nanoparticles in order to improve accumulation of magnetite nanoparticles in target cells, were used to magnetically label normal human dermal fibroblasts (NHDFs). Magnetically labeled NHDFs were seeded onto ultralow-attachment plates. When a magnet was placed under the plate, cells accumulate on the bottom of the well. After a 24-h-incubation period, the cells form a sheet-like structure, which contains the major dermal extracellular matrix (ECM) components (fibronectin and type I collagen) within the NHDF sheet. Human umbilical vein endothelial cells (HUVECs) were co-cultured with NHDF sheets by two methods: HUVECs and NHDFs were mixed and then allowed to form cell sheets by Mag-TE; or NHDF sheets were constructed by Mag-TE and HUVECs were subsequently seeded onto NHDF sheets. These methods gave tube-like formation of HAECs, resembling early capillaries, within or on the surface NHDF sheets after short-term 3D co-culture, thus suggesting that Mag-TE may be useful for constructing 3D-tissue involving capillaries.

Introduction

Tissue engineering is a promising technology for repairing defective tissues *in vivo*. Tissue engineering can be used to restore, or enhance the function of defective tissues. There are three main approaches to tissue engineering: (1) to use isolated cells and/or cell substitutes as cellular replacement parts, (2) to use acellular biomaterials capable of inducing tissue regeneration, and (3) to use a combination of cells and materials. Tissue engineering is generally based on the seeding of cells onto three-dimensional (3D) porous biodegradable scaffolds for constructing 3D tissue structures (Langer and Vacanti, 1993). These scaffolds allow the cells to form a 3D tissue structure via cell adhesion, proliferation and deposition of extracellular matrix (ECM). Problems with this approach include insufficient cell migration into the scaffolds, which may cause a crucial prolongation of the culture period due to a shortage of initially seeded cells, and inflammatory reactions to byproducts of scaffold biodegradation. To overcome these disadvantages, novel alternative approaches to creating 3D tissue constructs are needed.

Magnetite particles of nanometer to submicron size have been used in an increasing number of biological and medical applications (Shinkai and Ito, 2004). The unique feature of the magnetite particle is its reaction to magnetic force. Magnetite particles have been used for cell sorting, as high magnetic flux density attracts magnetically labeled cells (Miltenyi *et al.*, 1990; Radbruch *et al.*, 1994; Moore *et al.*, 1998; Lewin

Received on May 29, 2006. Correspondence concerning this article should be addressed to H. Honda (E-mail address: honda@nubio.nagoya-u.ac.jp).

et al., 2000). We previously developed magnetite cationic liposomes (MCLs), which contain 10-nm magnetite nanoparticles, in order to improve accumulation of magnetite nanoparticles in target cells, due to electrostatic interaction between MCLs and the cell membrane (Shinkai *et al.*, 1996). In addition, we recently developed a novel tissue engineering technique using MCLs, based on the fact that cells labeled with MCLs can be manipulated using magnetic force (Ito *et al.*, 2004a, 2004c, 2005a, 2005c; Shimizu *et al.*, 2005). With this technique, we used a magnet to accumulate magnetically labeled keratinocytes onto a culture surface, and sheet-like multi-layered 3D constructs were successfully created without using any artificial polymer scaffolds (Ito *et al.*, 2004a). Thus, we developed a novel methodology for tissue engineering using magnetite nanoparticles and magnetic force, which we designated "magnetic force-based tissue engineering (Mag-TE)".

Neovascularization is a critical obstacle yet to be overcome in the engineering of tissue constructs larger than a few cubic millimeters. Thick and large 3D tissue constructs require vascularization *in vitro*, which is able to maintain cell viability during tissue growth, induce structural organization and promote vascularization after implantation. Thus, it is necessary to develop a novel methodology to construct 3D tissues involving capillaries. In the present study, we investigated whether angiogenesis could be induced in 3D tissues constructed by Mag-TE. Angiogenesis is a complex process involving numerous growth factors, extracellular matrix (ECM) (Sengar, 1996; Sephel *et al.*, 1996), enzymes (Lorimier *et al.*, 1996; Weckoth *et al.*, 1996) and co-existing cell types *in vivo* (Schaffer and Nanney, 1996). In the present study, we investigated whether ECM components, such as type I collagen and fibronectin, which have the capacity to induce angiogenesis, are deposited in normal human dermal fibroblast (NHDF) sheets constructed by Mag-TE, and whether human umbilical vein endothelial cells (HUVECs) form capillaries during 3D co-culture with NHDF sheets. Furthermore, we periodically observed these capillaries in details, and show the processes of capillary formation were similar to that during early angiogenesis *in vivo*.

1. Materials and Methods

1.1 Cells and culture

HUVECs, NHDFs and normal human epidermal keratinocytes (NHEKs) were provided as frozen cells after primary culture by the supplier (Kurabo Industries Ltd.), and were cultured in commercially available growth media (HuMedia-EG2 for HUVECs, Medium106S for NHDFs, and HuMedia-KG2 for NHEKs; Kurabo) at 37°C in a humidified atmosphere of CO_2 and 95% air.

1.2 Preparation of magnetite cationic liposomes

Magnetite (Fe_3O_4; average particle size, 10 nm; Toda Kogyo) was used as the core of the MCLs. MCLs were prepared using colloidal magnetite and a lipid mixture of *N*-(α-trimethylammonioacetyl)-didodecyl-D-glutamate chloride (TMAG, a cationic lipid; Sogo Pharmaceutical Co.), dilauroylphosphatidyl-choline (DLPC; Sigma Chemical Co.), and dioleoylphosphatidyl-ethanolamine (DOPE; Avanti Polar Lipids Inc.) in a molar ratio of 1:2:2, as described previously (Shinkai *et al.*, 1996). Average MCL particle size was 150 nm, and was measured using a dynamic light scattering spectrophotometer (FRAR 1000, Otsuka Electronics Co., Ltd.).

1.3 MCL uptake by cells

Uptake of MCLs by HUVECs or NHDFs was examined as described previously (Shinkai *et al.*, 1996). Briefly, HUVECs or NHDFs were seeded into a 60-mm cell culture dish (Asahi Techno Glass Corp.). After a 24-h incubation period, the medium was replaced with MCL-containing medium (net magnetite concentration, 100 pg/cell) and cells were incubated further. To assay magnetite uptake, cells were sampled periodically, and iron concentration and the number of viable cells were measured using the potassium thiocyanate method (Owen and Sykes, 1984) and the dye-exclusion method with trypan blue, respectively.

1.4 Construction of cell sheets using MCLs and magnetic force (Mag-TE)

NHDFs were cultured until subconfluent, and medium were replaced with flesh medium containing MCLs (net magnetite concentration, 100 pg/cell). After 24 h of culture with MCLs, the medium were removed, and the cells were rinsed with phosphate-buffered saline (PBS) to remove the medium completely. Then, the cells were harvested by trypsin treatment. Magnetically labeled NHDFs (2×10^6 cells) were seeded into a 24-well ultralow-attachment plate (culture area, 200 mm^2, Corning Inc.), the surface of which is comprised of a covalently bound hydrogel layer that was hydrophilic and neutrally charged. A cylindrical neodymium magnet (diameter, 30 mm; height, 15 mm; magnetic induction, 0.40 T) was then placed at the reverse side of the ultralow-attachment plate in order to provide magnetic force vertical to the plate, and cells were cultured for 1 d. We designated this procedure "Mag-TE".

1.5 Construction of NHDF sheets by mixing HUVECs with NHDFs

In order to label cells magnetically, MCLs (net magnetite concentration, 100 pg/cell) were added to both NHDFs and HUVECs and cells were incubated for 24 h. Cells were harvested, and HUVECs (6×10^4 cells) were mixed with NHDFs (1.8×10^6 cells). The mixture was seeded onto ultra-low-attachment plates. A cylindrical neodymium magnet was then placed at the reverse side of the plate in order to provide magnetic

force vertical to the plate, and the cells were cultured for 1 d, allowing the formation of an NHDF sheet containing HUVECs.

1.6 Construction of vascularized NHDF sheets by seeding HUVECs onto NHDF sheets

Using the Mag-TE method described above, NHDF sheets without HUVECs were constructed. Subsequently, HUVECs (5×10^4 cells) or NHEKs (1.5×10^5 cells, control) were seeded onto NHDF sheets. Sheets were cultured in HuMedia-EG2 for 5 d in order to induce angiogenesis by HUVECs.

Fluorescence microscopy was performed using CellTracker™ (Molecular Probes); HUVECs and NHEKs were pre-stained with CMFDA (5-chloromethylfluoroscein diacetate; Molecular Probes), fluorescent-stained cells were seeded onto NHDF sheets and the formation of capillaries was periodically observed by fluorescence microscopy (Olympus Corp.). A time-course analysis of HUVEC areas was performed by the computerized image analysis of the number of pixels occupied by HUVEC-containing tubule areas ($n = 4$). Briefly, the image analysis of fluorescence images (image size, 1.21×10^6 pixels) was carried out using an image analysis program (Adobe Photoshop 6.0, Adobe Systems Inc.). Fluorescent areas (tubule areas) in the images were selected by magic wand tool, and the number of pixels occupied by tubule area was obtained.

1.7 Histology

For histological evaluation, cell sheets were washed with PBS, fixed in 10% formalin solution and embedded in paraffin. Thin (4 μm) slices were placed on silanized slides for immunohistochemistry or staining with hematoxylin-eosin (H&E). For immunohistochemistry, the primary antibodies used were rabbit anti-rat type I collagen (LSL), rabbit anti-human fibronectin (DakoCytomation), or anti-rabbit von Willebrand factor (vWF; DakoCytomation). Biotinylated goat anti-rabbit immunoglobulin (DakoCytomation) was used as a secondary antibody. Briefly, sections were incubated with 1% bovine serum albumin at 37°C for 30 min in order to block background staining, followed by incubation at 37°C for 60 min each with primary and secondary antibodies. Thereafter, slices were incubated at 37°C for 30 min with peroxidase-conjugated streptavidin (DakoCytomation). Each step was followed by washing with PBS. Peroxidase activity was visualized after soaking at room temperature for 10 min in 0.02% diaminobenzidine tetrahydrochloride containing 0.005% hydrogen peroxide (brown staining indicates peroxidase activity). Slides were also double-stained with Berlin blue (Ito *et al.*, 2004c) (blue staining indicates magnetite in MCLs). In negative control sections, primary antibodies were replaced with an unrelated monoclonal antibody.

For transmission electron microscopy, culture media were removed from the wells and were substituted with phosphate-buffered washing solution. Subsequent to all pre-embedding procedures, specimens were dehydrated in an ascending alcohol series. Fixed cells were then transferred and incubated in a propylene–epon mixture. From the embedded specimens, 1-μm serial sections were cut with an ultra-microtome (Ivan Sorvall) and were observed under a transmission electron microscope (H7000, Hitachi High-Technologies Corp.).

2. Results and Discussion

2.1 Magnetite nanoparticle uptake by cells and its effect on proliferation

The growth of NHDFs or HUVECs in medium containing MCLs (net magnetite concentration, 100 pg/cell) was compared with the growth in a medium without MCLs in order to investigate MCL toxicity against NHDFs or HUVECs. As shown in **Figure 1(a)**, MCLs did not inhibit the growth of NHDFs or HUVECs at the concentration studied.

As shown in Figure 1(**b**), the amounts of magnetite nanoparticles taken up by NHDFs and HUVECs differed; 24 h after the addition of MCLs, HUVECs took up 34 pg of magnetite per cell, whereas NHDFs took up 14 pg of magnetite per cell. Consequently, both cell types were sufficiently labeled magnetically to be attracted by a magnet (magnetic induction, 0.40 T). We reported previously that canine urothelial cells that took up 8 pg of magnetite per cell formed a sheet-like construct using the magnet (Ito *et al.*, 2005b). Therefore, we think that the NHDF sheet can be formed by Mag-TE. In subsequent experiments, MCLs were added to NHDFs or HUVECs at a concentration of 100 pg/cell, followed by a 24-h incubation period.

For clinical applications, MCL toxicity is an important issue. We previously reported that MCLs do not adversely affect proliferation of several types of normal cells within the range of MCL concentrations tested (i.e., human aortic endothelial cells [HAECs], <100 pg-magnetite/cell (Ito *et al.*, 2004c); human keratinocytes, <50 pg/cell (Ito *et al.*, 2004a); human smooth muscle cells, <100 pg-magnetite/cell (Ito *et al.*, 2005b); human mesenchymal stem cells [MSCs], <100 pg/cell (Ito *et al.*, 2004b)), and we observed no effects on MSC differentiation (Ito *et al.*, 2004b). However, further study is needed in order to assess the toxicity of residual magnetic nanopartilces in the grafts before Mag-TE can be used clinically.

2.2 Construction of NHDF sheets by Mag-TE

Magnetically labeled NHDFs were seeded onto 24-well ultralow-attachment plates and a 30-mm neodymium magnet was then placed under the plate. Because the magnetic density (0.40 T) was essentially even throughout the culture areas of the 24-well

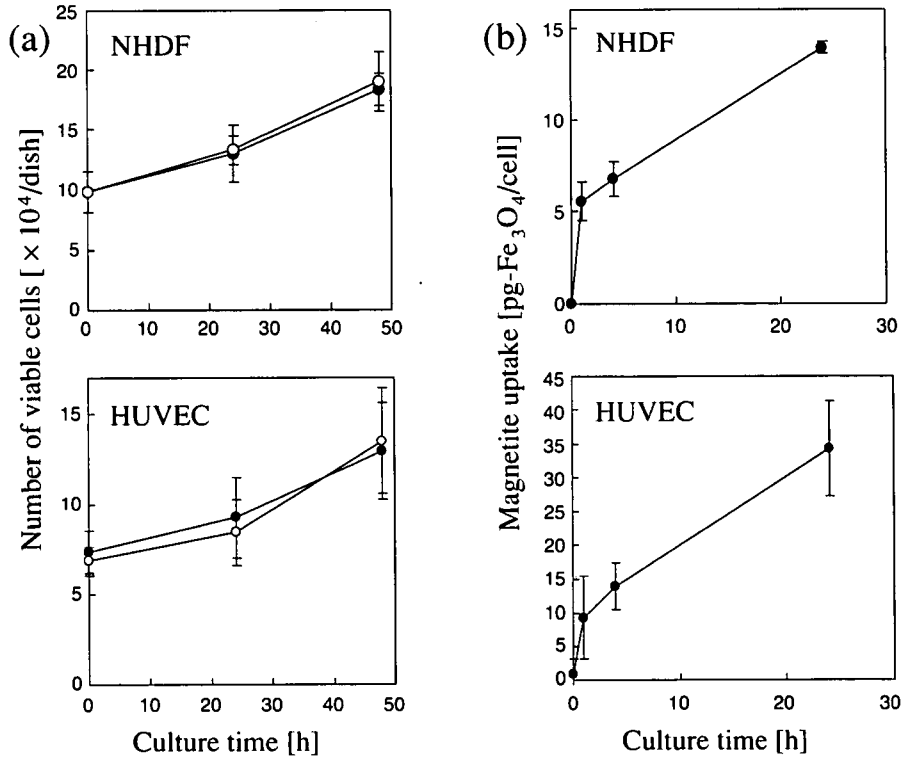

Fig. 1 MCL uptake and cell proliferation. MCL toxicity was examined by assessing cell growth after addition of MCLs (a). Open circles, no addition of MCLs; closed circles, addition of MCLs at 100 pg/cell. Magnetite nanoparticle uptake after addition of MCLs (100 pg/cell) was measured using the potassium thiocyanate method (b). Data points are means ± SD of duplicates

ultralow-attachment plates (Ito *et al.*, 2004a), NHDFs were rapidly attracted to the magnet and accumulated evenly over the bottom of the plate. After a 24-h incubation period, NHDF sediments shrank slightly and formed a sheet-like structure. In contrast, NHDFs without MCLs or with MCLs in the absence of a magnet did not form evenly contiguous cell sheets nor did they attach to the ultralow-attachment plates, but rather formed small spheroids (data not shown). **Figure 2(a)** shows an NHDF sheet constructed by Mag-TE; the sheets had a black-brown color, which is the color of magnetite. NHDF sheets constructed by Mag-TE shrank slightly (the decrease in the diameter was 20%) at 24 h after culture in the presence of a magnet. When the magnet was removed from the bottom of the plates, the sheets were detached from the bottom of the 24-well ultralow-attachment plates, and could be harvested without enzymatic digestion.

It has been observed and documented in 2D and 3D angiogenesis models using HUVEC that ECM components (type I collagen (Korff and Augustin, 1999), fibrin (Vailhe *et al.*, 1996), or matrigel (Kubota *et al.*, 1988)) promote capillary-like structure formation. Thus, ECM deposition is essential for constructing vascularized 3D tissues, particularly in scaffold-less cell sheets. It is generally difficult to fabricate 3D tissue constructs without using 3D scaffolds, due to the lack of cell adherence via cell–cell junctions, particularly in the vertical direction. This non-adherence may be caused by enzymatic digestion of ECM. To overcome this difficulty, Yamato *et al.* (2001) used a thermo-responsive culture surface grafted to poly (*N*-isopropylacrylamide) (PIPAAm), and recovered monolayer cell sheets grown on ECM deposited on the culture surface; because digestive enzymes were not used, the ECM remained intact and enhanced cell–cell attachment. Thus, this method of "cell sheet engineering" may be a viable alternative approach to tissue engineering. We developed a novel methodology, termed "Mag-TE", for the fabrication of cell sheets. We used magnetic attraction as a physical approach for enhancing layered cell–cell interactions.

We investigated whether ECM components were produced during NHDF sheet formation by Mag-TE. Cross-sectional observation by H&E staining revealed that NHDFs formed cell sheets of approximately 200 μm in thickness (Figure 2(b)) and containing Berlin blue-positive magnetite nanoparticles within the sheet (Figure 2(c)). Immunohistochemical staining revealed that ECM components such as fibronectin (Figure 2(d)) and type I collagen (Figure 2(e)), which are known to be major dermal ECM components and are known to promote capillary formation (Vailhe *et al.*, 2001), were deposited within the constructed NHDF sheets. Cell-ECM

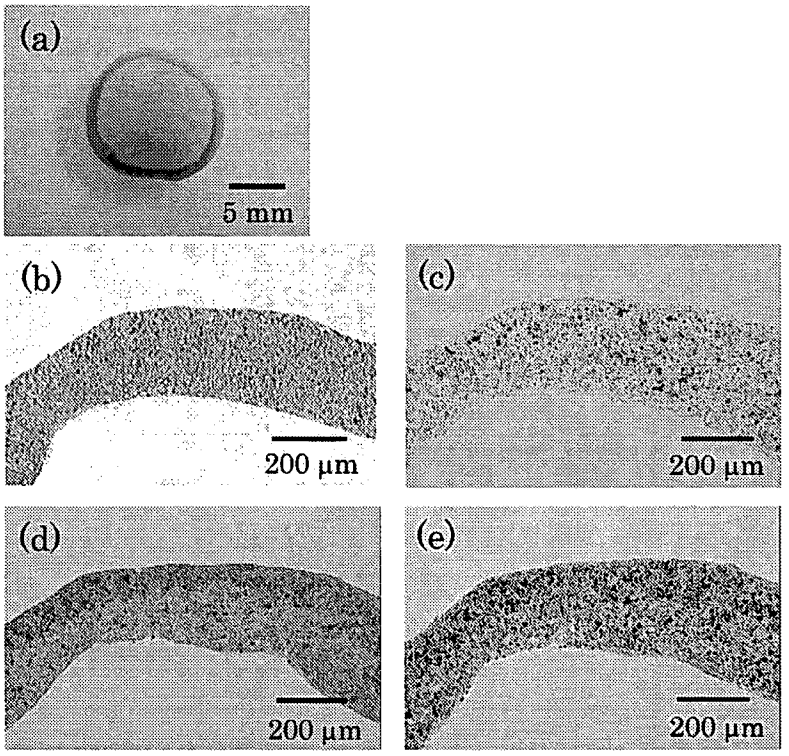

Fig. 2 Histological examination of fabricated NHDF sheets: (a) Bright-field micrograph of NHDF sheet constructed by Mag-TE; (b) Bright-field micrograph of hematoxylin/eosin-stained cross-sections of NHDF sheets constructed by Mag-TE; (c) Negative control using unrelated monoclonal antibody double-stained with Berlin blue (blue). Immunohistochemical stains for fibronection (brown, (d)) or type I collagen (brown, e) double-stained with Berlin blue (blue)

interactions can generate mechanical forces that can alter the structure of the surrounding ECM, which has been most convincingly shown in the case of fibroblast and $\alpha 2\beta 1$ integrin-mediated collagen gel contraction (Schiro *et al.*, 1991). These results suggest that collagen contraction due to NHDF-ECM interactions is involved in sheet shrinkage. The mechanism of ECM deposition remains to be elucidated, but we believe that the very close cell–cell interactions under 3D co-culture with magnetic force can elicit ECM deposition. ECM components deposited by cells within cell sheets during 3D-culture remain intact because the Mag-TE technique allows cell sheets to be harvested from the culture surface without enzymatic treatment. This point may play an important role in post-transplantation.

Fibroblasts are an integral component of all tissues; they contribute to architecture by producing ECM that serves as scaffolding for various organ structures, including vasculature. In addition, fibroblasts are a rich source of growth factors for self-stimulation and activation of other cell types in the microenvironment. In the present study, NHDF was selected as a model for construction of vascularized tissue, and two methods were employed in order to form capillaries *in* or *on* NHDF sheets.

2.3 Formation of capillaries in NHDF sheets

In order to produce capillaries within NHDF sheets, magnetically labeled NHDFs and HUVECs were admixed and seeded into ultralow-attachment plate. When the cells were co-cultured in the presence of a magnet for 1 d, NHDF sheets incorporating HUVECs were formed (overall appearance was as shown in Figure 2(a)). **Figure 3** shows cross-sections of NHDF sheets incorporating HUVECs on day 1. HUVECs formed tube-like structures with lumens of 5–6 μm (Figure 3(a)), and some formed connected tube-like structures (Figure 3(b)) within the sheets. Transmission electron microscopy revealed that HUVECs within NHDF sheets formed vacuoles (Figure 3(c)), suggesting that 3D co-culture of HUVECs within NHDF sheets induced angiogenesis.

2.4 Formation of capillaries on NHDF sheets

Alternatively, in order to construct capillaries on NHDF sheets, HUVECs were seeded onto NHDF sheets constructed by Mag-TE. **Figures 4(a)–(d)** show fluorescence microscopic images of HUVECs on NHDF sheets. HUVECs adhered to the NHDF sheets at 4 h after seeding (Figure 4(a)); extended on day 1 (Figure 4(b)); elongated and connected between cells on day 2 (Figure 4(c)); and finally organized into network structures, which exhibited multiple branching

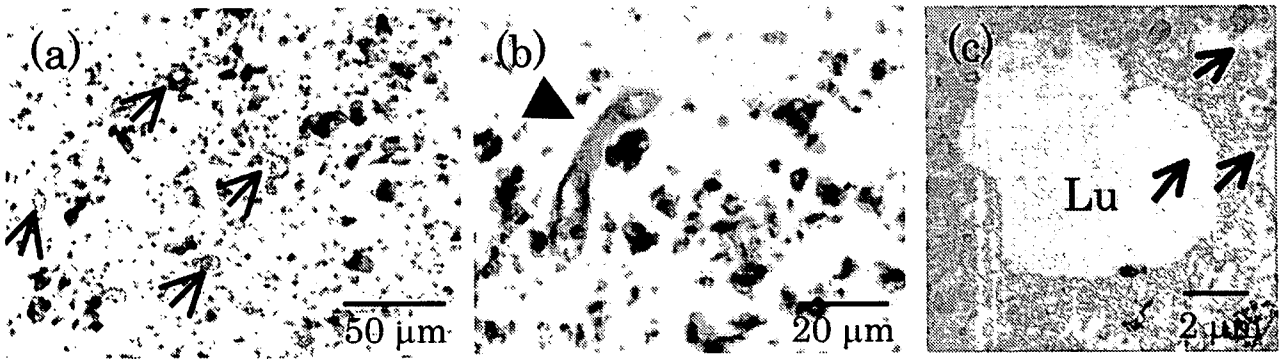

Fig. 3 Histological examination of HUVECs within NHDF sheets. Magnetically labeled NHDFs and HUVECs were admixed and seeded onto an ultralow-attachment plate, followed by placement of a magnet under the plate and coculture for 1 d. Bright-field micrographs of cross-sections of the cell sheets stained against vWF double-stained with tube-like structures and connection of two tube-like structures, respectively. (c) Transmission electron microscopy of cross-sections of fabricated cell sheets. Lumen (Lu) was evident. Arrows indicate magnetite particles

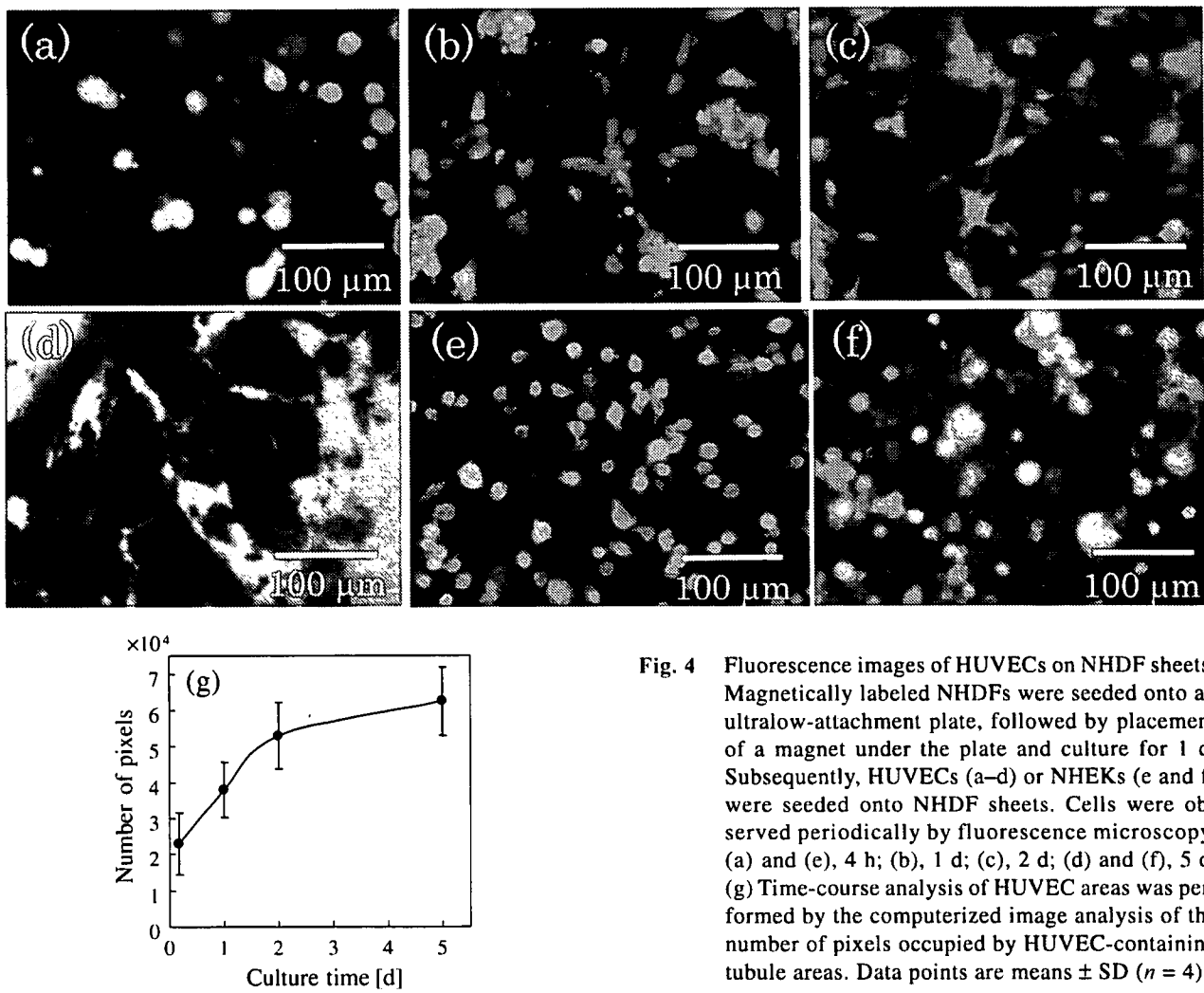

Fig. 4 Fluorescence images of HUVECs on NHDF sheets. Magnetically labeled NHDFs were seeded onto an ultralow-attachment plate, followed by placement of a magnet under the plate and culture for 1 d. Subsequently, HUVECs (a–d) or NHEKs (e and f) were seeded onto NHDF sheets. Cells were observed periodically by fluorescence microscopy. (a) and (e), 4 h; (b), 1 d; (c), 2 d; (d) and (f), 5 d. (g) Time-course analysis of HUVEC areas was performed by the computerized image analysis of the number of pixels occupied by HUVEC-containing tubule areas. Data points are means ± SD (n = 4)

points, on day 5 (Figure 4(d)). Time-course analysis of HUVEC areas was performed by computerized image analysis of the number of pixels occupied by HUVECs including tubule areas; the fluorescence area on the NHDF sheets increased (Figure 4(g)), thus suggesting that HUVECs proliferated and/or spread on the NHDF sheets for 5 d. On the other hand, although NHEKs adhered on the NHDF sheets at 4 h after

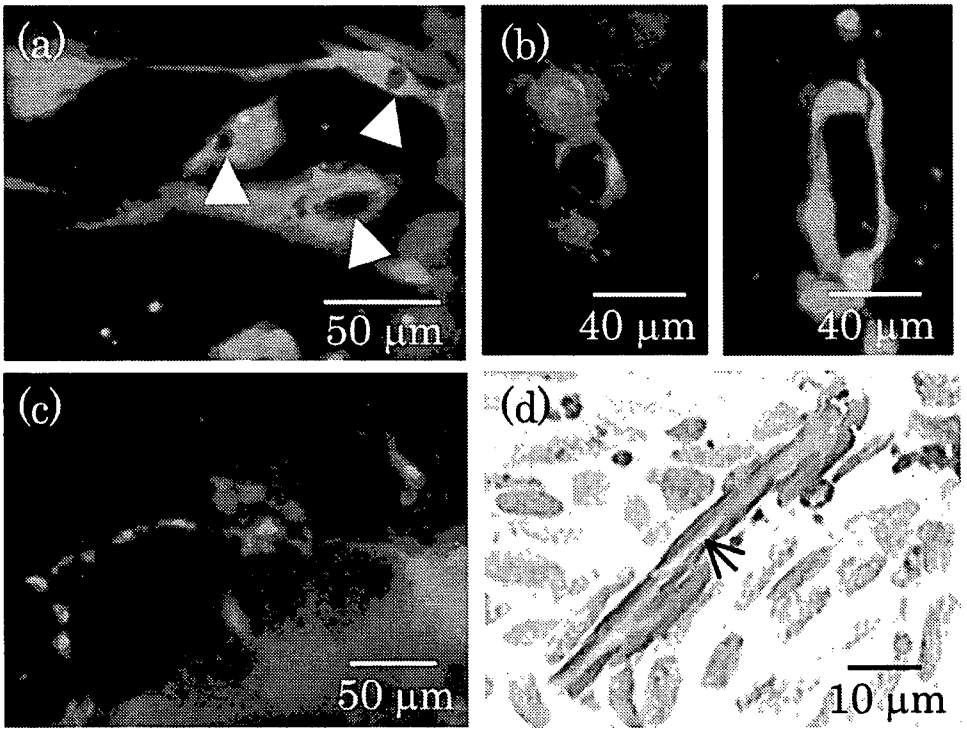

Fig. 5 Morphological changes of HUVECs on NHDF sheets. Fluorescence microscopy of HUVECs revealed vacuole (a, day 3, indicated by arrowheads) and lumen formation (b) consisting of two (left, day 5) or more cells (right, day 3), and sprouting of cord-like structures (c, day 5) on NHDF sheets. (d) Bright-field micrographs of immuno-staining against vWF (brown) double-stained with Berlin blue (blue) in thin slices (4 μm) of sheets revealed capillary lumen formation (indicated by an arrow) by HUVECs

co-culture (Figure 4(e)) and slightly increased in the cell number (data not shown), NHEKs did not organize cordlike network structures even after a 5-d culture period (Figure 4(f)).

Two major morphologic changes that regulate HUVEC tube development include lumen formation and sprouting, and these changes control how HUVECs interconnect into 3D networks. Fluorescence microscopic images of HUVECs co-cultured on NHDF sheets revealed vacuoles (**Figure 5(a)**) and lumens consisting of two or three HUVECs (Figure 5(b)), as well as sprouting with long cord-like structures (>250 μm, Figure 5(c)). Immuno-staining against vWF on thin slices (4 μm) of the sheets revealed capillary lumen formation surrounded by HUVECs (Figure 5(d)).

Tube-like formations of HUVECs were observed in both cases (Figures 3–5) after short-term 3D co-culture, but there may be differences between two methods with regard to the angiogenesis process. HUVECs incorporated within the NHDF sheets formed tube-like structures on day 1 (Figure 3), but the cross-sectional analysis revealed that the number of vWF-positive tube-like structures did not increase until at least 5 d after co-culture (data not shown). On the other hand, when HUVECs were seeded onto NHDF sheets, HUVECs proliferated and/or spread during the 5-d incubation period (Figure 4(g)). We suppose that the poor growth of HUVECs within the NHDF sheet was mainly caused by contact inhibition, i.e., HUVECs could not spread in the highly dense NHDF sheets.

In the present study, we showed that NHDF sheets constructed by Mag-TE induced HUVECs to generate a primitive cord-like network (Figure 4(d)), via vacuole (Figure 5(a)) and lumen formation (Figure 5(b)), and sprouting (Figure 5(c)), which mimic the processes observed during early angiogenesis *in vivo*. For application to tissue engineering, transplantation of preformed capillary structures may be crucial for graft survival. HUVEC-derived cords formed in 3D collagen gels have been shown to survive and inosculate with mouse microvessels after transplantation (Schechner *et al.*, 2000). Because blood vessels are stabilized by association with pericytes, including embryonic fibroblasts (Levenberg *et al.*, 2005) or smooth muscle cells, co-culture of these cells may be a possible approach. Previously, we succeeded in constructing Mag-tissue engineered small-diameter vascular tissue consisting of heterotypic layers of endothelial cells, smooth muscle cells and fibroblasts (Ito *et al.*, 2005b). Thus, the Mag-TE technique can be applied to construct a vascularized NHDF sheets incorporating pericytes or smooth muscle cells for vascular stabilization after transplantation. Furthermore, Mag-TE technique can be used for micro-patterning of

target cells, including HUVECs (unpublished results). Thus, we believe that designed capillaries can be formed on NHDF sheets by using micro-patterned magnets, and we are planning to construct native-like thick 3D structures consisting of multi-layer of the sheet.

Conclusions

We developed a novel methodology to construct vascularized cell sheets using MCLs and magnetic force ("Mag-TE"). Mag-TE allowed the *in vitro* fabrication and harvesting of NHDF sheets containing ECM and capillaries, and this technique may be applied to the engineering of thick 3D tissues for nutrient or oxygen supply.

Acknowledgment

This work was supported in part by the 21st Century COE Program 'Nature-Guided Materials Processing' and by a Grant-in-Aid for Scientific Research (No. 17760622) and by a Grant-in-Aid for Scientific Research on Priority Areas (No. 17066003) from the Ministry of Education, Sports, Science and Technology, Japan.

Literature Cited

Ito, A., M. Hayashida, H. Honda, K. Hata, H. Kagami, M. Ueda and T. Kobayashi; "Construction and Harvest of Multilayered Keratinocyte Sheets Using Magnetite Nanoparticles and Magnetic Force," *Tissue Eng.*, **10**, 873–880 (2004a)

Ito, A., E. Hibino, H. Honda, K. Hata, H. Kagami, M. Ueda and Kobayashi; "A New Methodology of Mesenchymal Stem Cell Expansion Using Magnetic Nanoparticles," *Biochem. Eng. J.*, **20**, 119–125 (2004b)

Ito, A., Y. Takizawa, H. Honda, K. Hata, H. Kagami, M. Ueda and T. Kobayashi; "Tissue Engineering Using Magnetite Nanoparticles and Magnetic Force: Heterotypic Layers of Cocultured Hepatocytes and Endothelial Cells," *Tissue Eng.*, **10**, 833–840 (2004c)

Ito, A., K. Ino, T. Kobayashi and H. Honda; "The Effect of RGD Peptide-Conjugated Magnetite Cationic Liposomes on Cell Growth and Cell Sheet Harvesting," *Biomaterials*, **26**, 6185–6193 (2005a)

Ito, A., K. Ino, M. Hayashida, T. Kobayashi, H. Matsunuma, H. Kagami, M. Ueda and H. Honda; "Novel Methodology for Fabrication of Tissue-Engineered Tubular Constructs Using Magnetite Nanoparticles and Magnetic Force," *Tissue Eng.*, **11**, 1553–1561 (2005b)

Ito, A., E. Hibino, C. Kobayashi, H. Terasaki, H. Kagami, M. Ueda, T. Kobayashi and H. Honda; "Construction and Delivery of Tissue-Engineered Human Retinal Pigment Epithelial Cell Sheets Using Magnetite Nanoparticles and Magnetic Force," *Tissue Eng.*, **11**, 489–496 (2005c)

Korff, T. and H. G. Augustin; "Tensional Forces in Fibrillar Extracellular Matrices Control Directional Capillary Sprouting," *J. Cell Sci.*, **112**, 3249–3258 (1999)

Kubota, Y., H. K. Kleinman, G. R. Martin and T. J. Lawley; "Role of Laminin and Basement Membrane in the Morphological Differentiation of Human Endothelial Cells into Capillary-Like Structures," *J. Cell Biol.*, **107**, 1589–1598 (1988)

Langer, R. and J. P. Vacanti; "Tissue Engineering," *Science*, **260**, 920–926 (1993)

Levenberg, S., J. Rouwkema, M. Macdonald, E. S. Garfein, D. S. Kohane, D. C. Darland, R. Marini, C. A. van Blitterswijk, R. C. Mulligan, P. A. D'Amore and R. Langer; "Engineering Vascularized Skeletal Muscle Tissue," *Nat. Biotechnol.*, **23**, 879–884 (2005)

Lewin, M., N. Carlesso, C. H. Tung, X. W. Tang, D. Cory, D. T. Scadden and R. Weissleder; "Tat Peptide-Derivatized Magnetic Nanoparticles Allow *in vivo* Tracking and Recovery of Progenitor Cells," *Nat. Biotechnol.*, **18**, 410–414 (2000)

Lorimier, S., P. Gillery, W. Hornebeck, F. Chastang, D. Laurent-Maquin, S. Bouthors, C. Droulle, G. Potron and F. X. Maquart; "Tissue Origin and Extracellular Matrix Control Neutral Proteinase Activity in Human Fibroblast Three-Dimensional Cultures," *J. Cell Physiol.*, **168**, 188–198 (1996)

Miltenyi, S., W. Muller, W. Weichel and A. Radbruch; "High Gradient Magnetic Cell Separation with MACS," *Cytometry*, **11**, 231–238 (1990)

Moore, L. R., M. Zborowski, L. Sun and J. J. Chalmers; "Lymphocyte Fractionation Using Immunomagnetic Colloid and a Dipole Magnet Flow Cell Sorter," *J. Biochem. Biophys. Methods*, **37**, 11–33 (1998)

Owen, C. S. and N. L. Sykes; "Magnetic Labeling and Cell Sorting," *J. Immunol. Methods*, **73**, 41–48 (1984)

Radbruch, A., B. Mechtold, A. Thiel, S. Miltenyi and E. Pfluger; "High-Gradient Magnetic Cell Sorting," *Methods Cell Biol.*, **42**, 387–403 (1994)

Schaffer, C. J. and L. B. Nanney; "Cell Biology of Wound Healing," *Int. Rev. Cytol.*, **169**, 151–181 (1996)

Schechner, J. S., A. K. Nath, L. Zheng, M. S. Kluger, C. C. Hughes, M. R. Sierra-Honigmann, M. I. Lorber, G. Tellides, M. Kashgarian, A. L. Bothwell and J. S. Pober; "*In vivo* Formation of Complex Microvessels Lined by Human Endothelial Cells in an Immunodeficient Mouse," *Proc. Natl. Acad. Sci., USA*, **97**, 9191–9196 (2000)

Schiro, J. A., B. M. Chan, W. T. Roswit, P. D. Kassner, A. P. Pentland, M. E. Hemler, A. Z. Eisen and T. S. Kupper; "Integrin Alpha 2 Beta 1 (VLA-2) Mediates Reorganization and Contraction of Collagen Matrices by Human Cells," *Cell*, **67**, 403–410 (1991)

Sengar, R. D.; "Molecular Framework for Angiogenesis: a Complex Web of Interactions between Extravasated Plasma Proteins and Endothelial Cell Proteins Induced by Angiogenesis Cytokines," *Am. J. Path.*, **149**, 1–7 (1996)

Sephel, G. C., R. Kennedy and S. Kudravi; "Expression of Capillary Basement Membrane Components during Sequential Phases of Wound Angiogenesis," *Matrix Biol.*, **15**, 263–279 (1996)

Shimizu, K., A. Ito and H. Honda; "Enhanced Cell-Seeding into 3D Porous Scaffolds by Use Magnetite Nanoparticles," *J. Biomed. Mater. Res. B. Appl. Biomater.*, **77**, 265–272 (2005)

Shinkai, M. and A. Ito; "Functional Magnetic Particles for Medical Application," *Adv. Biochem. Eng. Biotechnol.*, **91**, 191–220 (2004)

Shinkai, M., M. Yanase, H. Honda, T. Wakabayashi, J. Yoshida and T. Kobayashi; "Intracellular Hyperthermia for Cancer Using Magnetite Cationic Liposomes: *in vitro* Study," *Jpn. J. Cancer Res.*, **87**, 1179–1183 (1996)

Vailhe, B., X. Ronot, M. Lecomte, N. Wiernsperger and L. Tranqui; "Description of an *in vitro* Angiogenesis Model Designed to Test Antiangiogenic Molecules," *Cell Biol. Toxicol.*, **12**, 341–344 (1996)

Vailhe, B., D. Vittet and J. J. Feige; "*In vitro* Models of Vasculogenesis and Angiogenesis," *Lab. Invest.*, **81**, 439–452 (2001)

Weckoth, M., A. Vaheri, J. Lauharanta, T. Sorsa and Y. T. Konttinen; "Matrix Metalloproteinases, Gelatinase and Collagenase, in Chronic Leg Ulcers," *J. Invest. Dermatol.*, **106**, 1119–1124 (1996)

Yamato, M., M. Utsumi, A. Kushida, C. Konno, A. Kikuchi and T. Okano; "Thermo-Responsive Culture Dishes Allow the Intact Harvest of Multilayered Keratinocyte Sheets without Dispase by Reducing Temperature," *Tissue Eng.*, **7**, 473–480 (2001)

ELSEVIER

Biochemical Engineering Journal 33 (2007) 100–109

Biochemical Engineering Journal

www.elsevier.com/locate/bej

New cancer diagnosis modeling using boosting and projective adaptive resonance theory with improved reliable index

Hiro Takahashi [a,b,c], Yasuyuki Murase [a], Takeshi Kobayashi [d], Hiroyuki Honda [a,*]

[a] *Department of Biotechnology, School of Engineering, Nagoya University, Furo-cho, Chikusa-ku, Nagoya 464-8603, Japan*

[b] *Research Fellow of the Japanese Society for the Promotion of Science (JSPS), Japan*

[c] *Genetics Division, National Cancer Center Research Institute, 5-1-1 Tsukiji, Chuo-ku, Tokyo 104-0045, Japan*

[d] *School of Bioscience and Biotechnology, Chubu University, Matsumoto-cho 1200, Kasugai, Aichi 487-8501, Japan*

Received 22 April 2006; received in revised form 20 June 2006; accepted 5 August 2006

Abstract

An optimal and individualized treatment protocol based on accurate diagnosis is urgently required for the adequate treatment of patients. For this purpose, it is important to develop a sophisticated algorithm that can manage large amount of data, such as gene expression data from DNA microarray, for optimal and individualized diagnosis. Especially, marker gene selection is essential in the analysis of gene expression data.

In the present study, we developed the combination method of projective adaptive resonance theory and boosted fuzzy classifier with SWEEP operator method for model construction and marker selection. And we applied this method to microarray data of acute leukemia and brain tumor. The method enabled the selection of 14 important genes related to the prognosis of the tumor. In addition, we proposed improved reliability index for cancer diagnostic prediction of blinded subjects. Based on the index, the discriminated group with over 90% prediction accuracy was separated from the others.

PART-BFCS with improved RI_{BFCS} method does not only show high performance, but also has the feature of reliable prediction further. This result suggests that PART-BFCS with improved RI_{BFCS} method has the potential to function as a new method of class prediction for diagnosis of patients.

Keywords: Cancer diagnosis; Fuzzy classifier; Projective adaptive resonance theory; Marker gene selection; Reliability index

1. Introduction

Cancer is a major cause of disease related to human deaths in many developed countries. Frequently, the prognosis of cancer patients with the same clinical diagnosis can be different. Therefore, it is important that the prognosis of cancer patients is accurately determined, and an adequate treatment is proposed. However, the sensitivity of cancer patients to radiotherapy and/or chemotherapy is determined by complex causality involving multiple factors, and not a single factor because the mechanisms of cancer development (or malignancy) are extremely complex. Gene expression data from DNA microarray are individualized and are useful in the diagnosis and prognosis of diseases [1]. However, to conduct analysis, it is necessary to select significantly differentially expressed genes that are strongly related to diagnosis or prognosis of disease because the performance of classification analysis can decline due to such large quantities of data.

Feature selection has been performed in order to screen candidate genes for modeling. There are two types of approaches—wrapper approach and filter approach. In the former approach, features (genes) are selected as a part of mining algorithms, such as support vector machines (SVM) [2], fuzzy neural network (FNN) combined with SWEEP operator (FNN-SWEEP) method [1], and boosted fuzzy classifier with SWEEP operator (BFCS) method [3]. On the other hand, in the filter approach, features are selected by filtering methods, such as *U*-test, *t*-test, signal-to-noise statistic (S2N) [4] and projective adaptive resonance theory (PART) [5], prior to the application of mining algorithms.

These methods were often used alone in previous studies. In the present study, we combined various wrapper and filtering approaches and then, we applied these methods to gene expression profile data of leukemia and central nervous system tumor. It is necessary that specific and essential marker genes are selected for cancer classification and diagnosis. Minimum gene sets with-

* Corresponding author. Tel.: +81 52 789 3215; fax: +81 52 789 3214.
E-mail address: honda@nubio.nagoya-u.ac.jp (H. Honda).

1369-703X/$ – see front matter © 2006 Elsevier B.V. All rights reserved.
doi:10.1016/j.bej.2006.08.004

out false positive ones should be extracted. Therefore, various methods were compared under the condition of small inputs. The combination method of PART and BFCS was the best under this condition.

2. Materials and methods

2.1. Data processing

We used two kinds of gene expression profiles. The first one is the gene expression profiles, obtained from http://www.genome.wi.mit.edu/cgi-bin/cancer/datasets.cgi, reported by Golub et al. [4]. The data set comprised 7129 human genes (probe sets) and 72 patients (47 acute lymphoblastic leukemia (ALL) and 25 acute myeloid leukemia (AML)), which were obtained from acute leukemia patients at the first time of diagnosis. In this experiment, the data set was partitioned into one data set comprised of two groups: 38 patients (27 ALL, 11 AML) as a modeling data set for constructing the class prediction model (predictor) and 34 patients (20 ALL, 14 AML) as a blinded data set for evaluating the constructed predictor. We excluded those genes for which all the 72 patients showed an intensity of less than 1000 signals [6] prior to applying the various filtering methods. Thus, 2476 genes were selected for the present study.

The second one is gene expression data set of medulloblastoma, which is a type of central nervous system (CNS) tumor, obtained from http://www.genome.wi.mit.edu/MPR/CNS, reported by Pomeroy et al. [7]. Patients with medulloblastoma are treated by combinations of surgery, radiotherapy, and chemotherapy. In the present data set, the following three drugs are mainly used for chemotherapy: vincristine, cisplatin, and cytoxan. Therefore, by using gene selection and prognosis modeling proposed in the present study, the gene related to the treatment response can be extracted. The data set comprised 7129 human genes (probe sets) and 60 patients from whom tumor specimens were obtained by surgery. Among these 60 patients, a few patients (16) had a short follow-up period. Therefore, we used the data of the remaining 44 patients for the construction of a 4-year survival prediction model. Of these 44 patients, 26 patients remained alive after 4 years and 18 patients had died. In this experiment, the data set was randomly partitioned into three data sets consisting of two groups: 30 or 29 patients (18 or 17 survivors, 12 dead) as a modeling data set for constructing the class prediction model (predictor) and 14 or 15 patients (8 or 9 survivors, 6 dead) as a blinded data set for evaluating the constructed predictor. We excluded those genes for which all the 44 patients showed the intensity of less than 1000 signals prior to applying the various filtering methods. Thus, 2713 genes were selected for the present study.

In order to validate performance of models, 10 independent predictors were constructed from these genes by the parameter increasing method (PIM). The prediction accuracy of the blinded data set was utilized for comparison of model performance, and the accuracy was calculated as the average of 10 independent combination predictors.

A total of 1000 genes were selected by various gene screening methods, e.g. Mann—Whitney's U-test, signal-to-noise statistic (S2N), and projective adaptive resonance theory (PART), prior to the model construction step. Subsequently, various modeling methods were applied as described in the following sections.

2.2. Determination of optimal input number

When a large number of inputs are provided in the model, the model is excess fitted to the training data and the robustness is lost. Therefore, in order to construct a model with relatively high robustness, we assumed that the number of IF-THEN rules should not exceed the sample number [1]. Then, we used a stopping condition in the present study such that the total input number became $N_{\text{attribute}}$ in all the selected weak learners; $N_{\text{attribute}}$ is defined according to the following condition:

$$N_{\text{attribute}} < \log_2 N \tag{1}$$

where $N_{\text{attribute}}$ indicates the optimum selected attribute number.

Using Eq. (1), $N_{\text{attribute}}$ is 4 since N is 30 (or 29) for the CNS data set and 5 since N is 38 for the leukemia data set.

2.3. Boosted fuzzy classifier with SWEEP operator (BFCS)

Boosting was proposed by Schapire [8], and thus far, several derivative boosting algorithms [9–11] have been developed. Boosting is useful for class prediction using high dimensional inputs and is very fast algorithms.

In the previous study, we developed a boosted fuzzy classifier with SWEEP operator (BFCS) method [3] on the basis of AdaBoost [9], which is the most basic boosting algorithm. This method enables the evaluation of reliability of the predictions for each patient. On the other hand, it is difficult to evaluate the reliability of the predicted results of the conventional boosting.

Fig. 1 shows the structure of BFCS. BFCS is composed of one-input type I fuzzy neural network (FNN) models [12]. In the present study, one-input FNN models were used as weak learners in the BFCS model, and they were combined by connection weights, which were determined by the AdaBoost algorithm. FNN has three types of weight parameters (w_c, w_g, and w_f) [12]. In the present study, parameter w_g is a constant value (=2.0 ln((1.0+0.995)/(1.0−0.995))) [12], and w_c is a threshold that has the best odds ratio in the case that only one input was used. w_c and w_g were determined; w_f was calculated by the SWEEP operator method [12].

2.3.1. Reliability index for BFCS (old RI_{BFCS})

Reliability index (RI) based on fuzzy inference has been proposed to evaluate the result of class prediction by Huang and Li [13]. We have developed a reliability index for BFCS (RI_{BFCS}) by modifying RI for boosting.

We modified RI equations as follows:

$$\text{RI}_{\text{BFCS}} = \begin{cases} \text{INT}(\text{diff}_{\text{BFCS}} \cdot 10) + 1, & \text{if } 0 \le \text{diff}_{\text{BFCS}} < 0.9 \\ 10, & \text{if } \text{diff}_{\text{BFCS}} \ge 0.9 \end{cases} \tag{2}$$

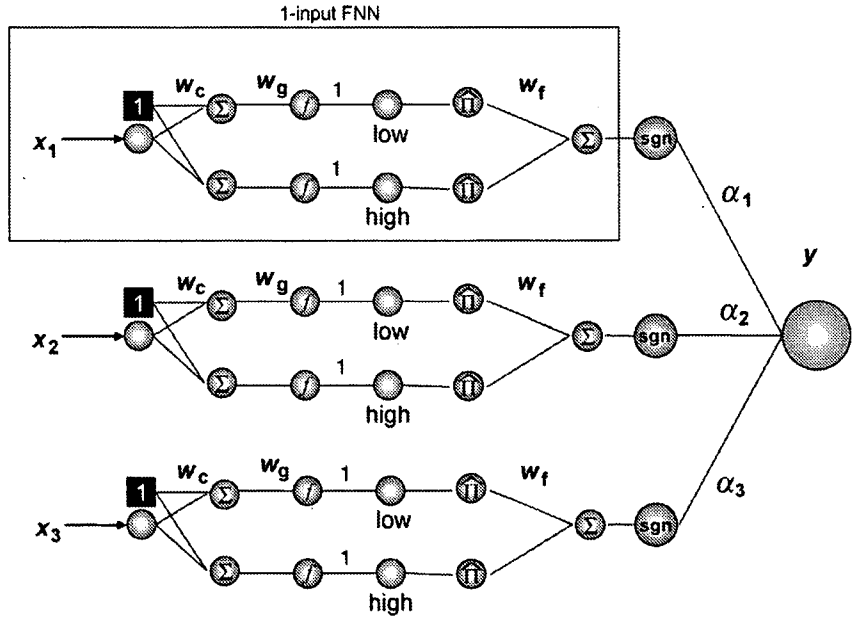

Fig. 1. Concept of the BFCS model.

where

$$\mathrm{diff}_{\mathrm{BFCS}} = \frac{\sum_t^T \left\{ \alpha_t \cdot \underset{v \in M_t}{\mathrm{argmin}}(\mathrm{diff}_v) \right\}}{\sum_t^T \alpha_t} \tag{3}$$

where T indicates the number of weak learners in the BFCS model, M_t indicates set of input variables in tth selected weak learner, α_t indicates the connection weight of the tth selected model in the construction of BFCS models, and diff_v is defined by the following equation:

$$\mathrm{diff}_v = u_{\mathrm{highest}}(X_v) - u_{\mathrm{next\ highest}}(X_v) \tag{4}$$

where v indicates the vth input in the BFCS model and $u(x_v)$ indicates the grade of the fuzzy membership function when the vth input x_v was inputted. It is defined by the following equation [12]:

$$u_v = \frac{1}{1 + \exp\{-w_g(x_v + w_c)\}} \tag{5}$$

$\mathrm{RI}_{\mathrm{BFCS}}$ is calculated for each example. Here, the greater $\mathrm{RI}_{\mathrm{BFCS}}$ the sample has, the more reliable its prediction.

2.3.2. Improved reliability index for BFCS (new RI_{BFCS})

In the present study, we propose improved reliability index by modifying equation of $\mathrm{RI}_{\mathrm{BFCS}}$ for more practical cancer diagnosis. For previous reliability index, argmin(diff_v)s in each weak learner, that mean distance from boundary line, are multiplied by α_t and summed. For improved reliability index, argmin(diff_v) in weak learner that output opposite to integrated model, is used as negative value. It is defined by the following equation:

$$\mathrm{diff}_{\mathrm{BFCS}} = \frac{\sum_t^T \left\{ \alpha_t \cdot g_t \cdot \underset{v \in M_t}{\mathrm{argmin}}(\mathrm{diff}_v) \right\}}{\sum_t^T \alpha_t} \tag{6}$$

where

$$g_t = \begin{cases} -1, & \text{if sign } (O_t) \neq \text{sign } (O_I) \\ +1, & \text{if sign } (O_t) = \text{sign } (O_I) \end{cases} \tag{7}$$

where O_t indicates output of tth model, and O_I indicates output of integrated model.

2.4. k-Nearest neighbor (kNN)

The k-nearest neighbor (kNN) methods are based on a distance function for pairs of tumor samples, such as the Euclidean distance. The kNN proceeds as follows to classify blind data set observations on the basis of the modeling data set. For each patient in the blind data set (a) finding the k-closest patients in the modeling data set and (b) predicting the class by majority vote; that is, choosing the class that is most common among those k-neighbors. The number of neighbors $k = 3$ was used because a similar cross-validation accuracy of model was obtained in the modeling data set for various k.

2.5. Multiple regression analysis (MRA)

The multiple regression analysis (MRA) is one of conventional methods. The MRA is a concerned with describing and evaluating the relationship between a patient's outcome and gene expression. MRA models are used to help us predict patient's outcome by using gene expression data.

2.6. Weighted voting (WV)

The weighted voting (WV) method was originally proposed by Golub et al. [4] to manage microarray data. The weights of each gene were calculated by the signal-to-noise. The linear models of one gene were assembled with gene weight.

2.7. Support vector machine (SVM)

The support vector machine (SVM) was originally proposed by Vapnik and Chervonenkis [14] and is used to avoid the "curse of dimensionality". SVM is superior to many other conventional methods and is frequently used in bioinformatics. In the present study, the SVM-LIGHT software package [15] was used. It was modified, and a PIM function was added to select a combination of inputs. In the present study, the regulatory parameter c was the default value of SVM_LIGHT ((avg(input vector)^2)$^{-1}$). A linear kernel was used because a similar cross-validation accuracy of model was obtained in the modeling data set for various kernels.

2.8. Fuzzy neural network (FNN) combined with SWEEP operator method (FNN-SWEEP)

The fuzzy neural network (FNN) combined with SWEEP operator method (FNN-SWEEP method) was also applied for model construction. The FNN-SWEEP method was originally proposed by Noguchi et al. [16] and was modified by Ando et al. [1] to manage microarray data. FNN has three types of weight parameters (w_c, w_g, and w_f) [12] as shown in Fig. 2. If w_c and w_g are fixed, FNN can be treated as multiple linear regression model in which w_f is variable parameter. Therefore, w_f was easily optimized without training. In the FNN-SWEEP method, only parameter w_f was optimized by the SWEEP operator method during the feature selection step. After the input combinations were determined, FNN models with the selected input combinations were optimized using a backpropagation algorithm on model construction step. In the backpropagation algorithm, the number of epochs was set to

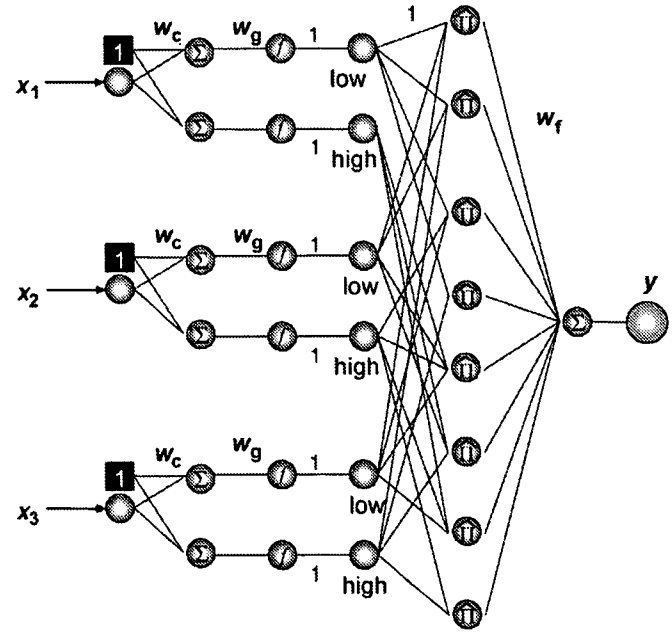

Fig. 2. Three-input type-I FNN model.

Table 1
Comparison of accuracies on various combination methods for leukemia data set (%)

	Inputs				
	1	2	3	4	5
BFCS with PART	77.9 ± 10.7	67.4 ± 7.6	84.7 ± 7.4	86.5 ± 4.4	89.1[a] ± 7.3
BFCS with S2N	78.8 ± 10.6	67.4 ± 7.6	84.4 ± 7.3	85.6 ± 5.7	83.2 ± 2.2
BFCS with *U*-test	78.8 ± 10.6	67.4 ± 7.6	84.4 ± 7.3	85.6 ± 5.7	83.2 ± 2.2
BFCS without screening	78.8 ± 10.6	67.4 ± 7.6	84.4 ± 7.3	85.6 ± 5.7	83.2 ± 2.2
SVM with PART	77.4 ± 10.0	79.4 ± 7.5	80.0 ± 8.2	80.9 ± 9.7	82.4 ± 8.4
SVM with S2N	76.2 ± 11.2	78.5 ± 7.0	81.8 ± 7.7	83.2 ± 9.0	82.4 ± 9.7
SVM with *U*-test	76.2 ± 11.2	78.5 ± 7.0	82.6 ± 6.2	84.1 ± 6.7	83.5 ± 8.0
SVM without screening	76.2 ± 11.2	78.5 ± 7.0	83.5 ± 6.2	84.7 ± 6.4	85.0 ± 7.7
FNN-SWEEP with PART	77.6 ± 12.2	77.1 ± 13.1	79.7 ± 9.1	80.3 ± 8.1	85.9 ± 7.7
FNN-SWEEP with S2N	77.9 ± 11.9	80.3 ± 7.8	81.8 ± 8.0	81.5 ± 8.2	81.5 ± 9.0
FNN-SWEEP with *U*-test	77.9 ± 11.9	80.3 ± 7.8	81.2 ± 7.5	82.6 ± 9.3	81.2 ± 8.5
FNN-SWEEP without screening	77.9 ± 11.9	80.3 ± 7.8	81.8 ± 8.0	84.4 ± 9.0	83.5 ± 8.7
*k*NN with PART	80.3 ± 11.8	75.3 ± 11.8	76.5 ± 11.8	80.0 ± 12.3	77.6 ± 12.5
*k*NN with S2N	79.1 ± 12.8	82.9 ± 12.8	82.6 ± 12.5	79.7 ± 9.8	79.4 ± 9.1
*k*NN with *U*-test	79.1 ± 12.8	84.1 ± 9.9	82.1 ± 9.0	81.5 ± 10.5	81.8 ± 10.8
*k*NN without screening	79.1 ± 12.8	79.4 ± 12.4	80.0 ± 11.3	78.8 ± 10.7	81.5 ± 9.3
MRA with PART	77.4 ± 11.2	79.4 ± 10.9	79.4 ± 10.3	75.3 ± 11.4	64.1 ± 8.2
MRA with S2N	77.9 ± 11.1	80.6 ± 8.8	83.2 ± 7.7	74.7 ± 9.6	64.7 ± 8.2
MRA with *U*-test	77.9 ± 11.1	80.6 ± 8.8	83.5 ± 8.0	76.2 ± 9.7	67.1 ± 7.0
MRA without screening	77.9 ± 11.1	80.6 ± 8.8	83.8 ± 8.2	76.2 ± 7.0	66.8 ± 6.8
WV with PART	79.7 ± 10.7	76.5 ± 12.5	82.4 ± 7.0	75.3 ± 8.6	72.4 ± 11.2
WV with S2N	78.2 ± 11.2	83.5 ± 7.5	70.9 ± 13.1	71.2 ± 12.6	70.6 ± 10.1
WV with *U*-test	78.2 ± 11.2	85.6 ± 5.8	76.2 ± 10.7	73.2 ± 14.2	76.2 ± 11.5
WV without screening	78.2 ± 11.2	78.8 ± 7.9	76.2 ± 13.6	77.1 ± 10.7	85.3 ± 9.4

The average blinded accuracies and their S.D.s were calculated from 10 combination models constructed by PIM.
[a] The highest accuracy.

5000, and the learning rate was set to 0.1, these values are the same as those reported by Ando et al. [1].

2.9. Model construction with parameter selection

The parameter increasing method (PIM) [17] was used to select input combinations for model construction of FNN-SWEEP, SVM, *k*NN, MRA, and WV. This was done as follows.

First, we predicted the subtype of each sample by using the prediction model with a single input. Prediction models for each probe were constructed in a series, and all the probes were ordered based on the accuracy of the constructed models. In the next step, the probe having the highest accuracy level was used for constructing a combination model.

Second, we selected a partner probe for the probe selected in the first step in order to increase the prediction accuracy. To accomplish this, we constructed a two-input model in which a ranked probe was designated as input 1, and input 2 (partner probe) was selected to provide the highest training accuracy while applying FNN-SWEEP (or SVM, *k*NN, MRA, and WV) and PIM to the modeling data. By repeating this step, a combination of $N_{\text{attribute}}$ candidate probes was identified for use as input probes in the model construction.

Finally, combinations of $N_{\text{attribute}}$ probes, i.e. from the first to the $N_{\text{attribute}}$th probe were evaluated. We constructed $N_{\text{attribute}}$ predictor models, beginning with one input using only the first-selected probe to $N_{\text{attribute}}$ inputs using all the $N_{\text{attribute}}$ probes. The predictor models were specifically constructed by using a backpropagation algorithm for FNN-SWEEP or quadratic programming for SVM. The performance of the prediction models was evaluated by applying them to the blinded data set.

For the two gene expression profile data, the genes with the first to the 10th highest accuracies were used as the first inputs for the construction of the 10 combination models by PIM. The S.D.s of blinded accuracies were calculated by using ones of these 10 combination models.

2.10. PART-BFCS method

Previously, we developed PART filtering method by modifying PART [18,19]. And, we developed and combined the PART filtering method as a gene filtering method and BFCS as a modeling method. In this PART-BFCS method, PART first preselects the genes that show small variances within a class. Then, BFCS rapidly selects these genes to build a highly accurate and reliable predictor.

PART has two important parameters, vigilance and distance parameters. The vigilance parameter was optimized so that modeling samples clustered well. The distance parameter was used to control the number of extracted genes. The genes extracted by PART showed low standard deviation (S.D.) in lower gene expression class. The predictor using genes with low S.D. in lower class showed high performance [5].

In BFCS model, one-input FNN models on the basis of neural network and fuzzy logic, were used as weak learners. FNN has three types of connection weights (w_c, w_g, and w_f). These parameters were optimized as mentioned in section of BFCS algorithm. The only one parameter that should be optimized is the number of input in boosting model. This parameter was optimized by using the number of samples.

Table 2
Frequency of construction of high performance model

	Methods	
	Leukemia[a]	CNS[b]
BFCS with PART	4/10	13/30
BFCS with S2N	0/10	3/30
BFCS with *U*-test	0/10	3/30
BFCS without screening	0/10	3/30
SVM with PART	2/10	2/30
SVM with S2N	1/10	2/30
SVM with *U*-test	2/10	0/30
SVM without screening	0/10	0/30
FNN-SWEEP with PART	0/10	3/30
FNN-SWEEP with S2N	0/10	0/30
FNN-SWEEP with *U*-test	0/10	0/30
FNN-SWEEP without screening	0/10	0/30
*k*NN with PART	0/10	0/30
*k*NN with S2N	0/10	0/30
*k*NN with *U*-test	0/10	0/30
*k*NN without screening	0/10	0/30
MRA with PART	0/10	0/30
MRA with S2N	0/10	0/30
MRA with *U*-test	0/10	0/30
MRA without screening	0/10	0/30
WV with PART	0/10	1/30
WV with S2N	0/10	2/30
WV with *U*-test	0/10	1/30
WV without screening	0/10	0/30

[a] Ten combination models from first to 10th models were constructed by PIM for each method in five-inputs. The accuracies of the models with first and second highest performance were 100% (=100 × 34/34) and 97.1% (=100 × 33/34), respectively. The number of the models with 100% or 97.1% accuracies were counted from 10 combination models.

[b] Ten combination models from first to 10th models were constructed by PIM for each method and each set (of three-fold cross-validation) in four-inputs. The accuracies of the models with first and second highest performance were 86.7% (=100 × 13/15) and 85.7% (=100 × 12/14), respectively. The number of the models with 86.7% or 85.7% accuracies, were counted from 30 combination models for three data sets.

3. Results and discussion

3.1. Comparison of the performance of PART-BFCS and the other methods

The performances of wrapper approaches with filter approaches as class predictors were investigated. For comparison, many combinations of various wrapper approaches, such as BFCS, SVM, FNN-SWEEP, *k*-nearest neighbor (*k*NN), multiple regression analysis (MRA), and weighted voting (WV), and various filtering approaches, such as *U*-test, S2N, PART, and no screening, were constructed. The performance of the predictors

Table 3
Comparison of cross-validation accuracies on various combination methods for CNS tumor data set (%)

	Inputs			
	1	2	3	4
BFCS with PART	65.6 ± 11.1	70.9 ± 14.3	74.5 ± 9.7	773[a] ± 8.8
BFCS with S2N	67.5 ± 11.5	67.4 ± 13.2	71.0 ± 9.7	71.1 ± 9.5
BFCS with *U*-test	67.5 ± 11.5	66.3 ± 12.8	71.2 ± 9.2	71.3 ± 9.1
BFCS without screening	67.5 ± 11.5	66.3 ± 12.8	71.2 ± 9.2	71.3 ± 9.1
SVM with PART	65.1 ± 14.9	65.6 ± 12.9	65.3 ± 12.9	65.8 ± 14.2
SVM with S2N	68.0 ± 11.6	66.8 ± 9.0	69.5 ± 8.1	68.3 ± 10.3
SVM with *U*-test	67.6 ± 11.9	66.3 ± 10.1	68.0 ± 8.8	65.7 ± 8.1
SVM without screening	67.6 ± 11.9	65.9 ± 9.6	68.2 ± 8.6	66.3 ± 10.0
FNN-SWEEP with PART	65.1 ± 11.3	66.5 ± 10.3	65.5 ± 12.6	62.2 ± 13.1
FNN-SWEEP with S2N	67.2 ± 12.6	62.9 ± 11.9	60.9 ± 10.4	59.1 ± 12.9
FNN-SWEEP with *U*-test	67.0 ± 12.6	62.5 ± 11.1	60.4 ± 10.1	59.1 ± 14.4
FNN-SWEEP without screening	67.0 ± 12.6	62.7 ± 10.6	60.3 ± 11.6	58.7 ± 11.9
*k*NN with PART	60.3 ± 11.6	59.3 ± 10.5	58.9 ± 12.2	59.8 ± 11.4
*k*NN with S2N	59.5 ± 11.9	57.2 ± 10.8	55.6 ± 10.9	55.0 ± 10.6
*k*NN with *U*-test	59.5 ± 10.9	58.6 ± 11.5	58.0 ± 9.9	57.1 ± 11.1
*k*NN without screening	58.0 ± 12.6	56.6 ± 11.7	57.5 ± 9.7	57.5 ± 9.0
MRA with PART	65.2 ± 11.2	64.2 ± 11.1	61.8 ± 14.6	55.2 ± 11.8
MRA with S2N	67.2 ± 11.9	63.3 ± 12.7	63.0 ± 10.9	56.9 ± 9.6
MRA with *U*-test	67.2 ± 11.9	61.8 ± 11.6	60.1 ± 10.4	55.1 ± 12.1
MRA without screening	67.2 ± 11.9	62.7 ± 11.3	59.1 ± 10.3	54.3 ± 13.6
WV with PART	61.7 ± 14.3	63.9 ± 12.9	60.9 ± 13.0	64.6 ± 12.0
WV with S2N	63.3 ± 13.8	63.3 ± 12.1	62.6 ± 12.1	63.1 ± 11.3
WV with *U*-test	66.1 ± 11.4	62.6 ± 9.3	62.3 ± 10.4	63.2 ± 10.1
WV without screening	66.1 ± 11.4	62.6 ± 11.4	63.0 ± 11.3	63.6 ± 9.6

The average blinded accuracies and their S.D.s were calculated from 10 combination models constructed by PIM.
[a] The highest accuracy.

was compared on the basis of the accuracy by using a blinded data set that was not used for modeling. By using 10 independent class predictor models, the average accuracy for blinded data set was calculated for the CNS and leukemia data sets.

The results of leukemia data are shown in Table 1. The result shows that average accuracy of the PART-BFCS models is the highest as shown in Table 1. In this experiment, top 10 independent class predictor models were constructed by PIM (parameter increasing method) [17] for each condition and data set. And the numbers of construction of high performance model (100% or 97.1% accuracy) were counted for each method as shown in Table 2. Four models among 10 models of five-input show 97.1% or more accuracy for PART-BFCS method. Next, the results for CNS data are shown in Table 3. The inputs used in the predictors were gradually increased from the one-input model to four-input model. As shown in Table 3, the PART-BFCS method clearly showed high performance when compared with the other methods in all input models with the exception of one-input model. The accuracy of the PART-BFCS method gradually increased and eventually, it reached 77.3% in the four-input models. On the other hand, SVM, FNN-SWEEP, *k*NN, MRA, and WV with various filtering showed an accuracy of 55.1–68.3%, which was lower than that of PART-BFCS. Average accuracy of three-input SVM models with S2N was the highest except BFCS models (69.5%). By using *U*-test, however, we found that the accuracy of BFCS with PART was significantly ($P = 5.94 \times 10^{-4}$) higher than one of SVM with S2N. In the four-input models, PART-BFCS method could constructed the most models that showed accuracies were 86.7% (first highest) or 85.7% (second highest), as shown in Table 2. These results could be explained by the facts that PART is the useful filtering method that could improve performances of simple models [5], BFCS is the modeling method in which the model is constructed by assembling simple models, such as one-input FNN. Otherwise, complex models are constructed by other modeling methods. Table 2 shows that the most high performance models were constructed by PART-BFCS method. Therefore, combination of PART and BFCS is the best one.

3.2. Evaluation of prediction results using improved RI_{BFCS}

PART-BFCS method can estimate assurance of results by calculating reliability index for BFCS (RI_{BFCS}). In the present study, we propose improved RI_{BFCS} (new RI_{BFCS}) by modifying equation of RI_{BFCS} (old RI_{BFCS}) for more practical cancer diagnosis. For acute leukemia and CNS data, both RI_{BFCS} of each patient in blinded data were calculated (Fig. 3). Fig. 3 shows distributions of correct and incorrect sample for old and new RI_{BFCS}. It is necessary that there are many incorrect samples in low RI_{BFCS} and many correct samples in high RI_{BFCS}. For old RI_{BFCS}, two distributions are not separated ($P = 0.169$, 0.311), as shown in Fig. 3A and B. On the other hand, they

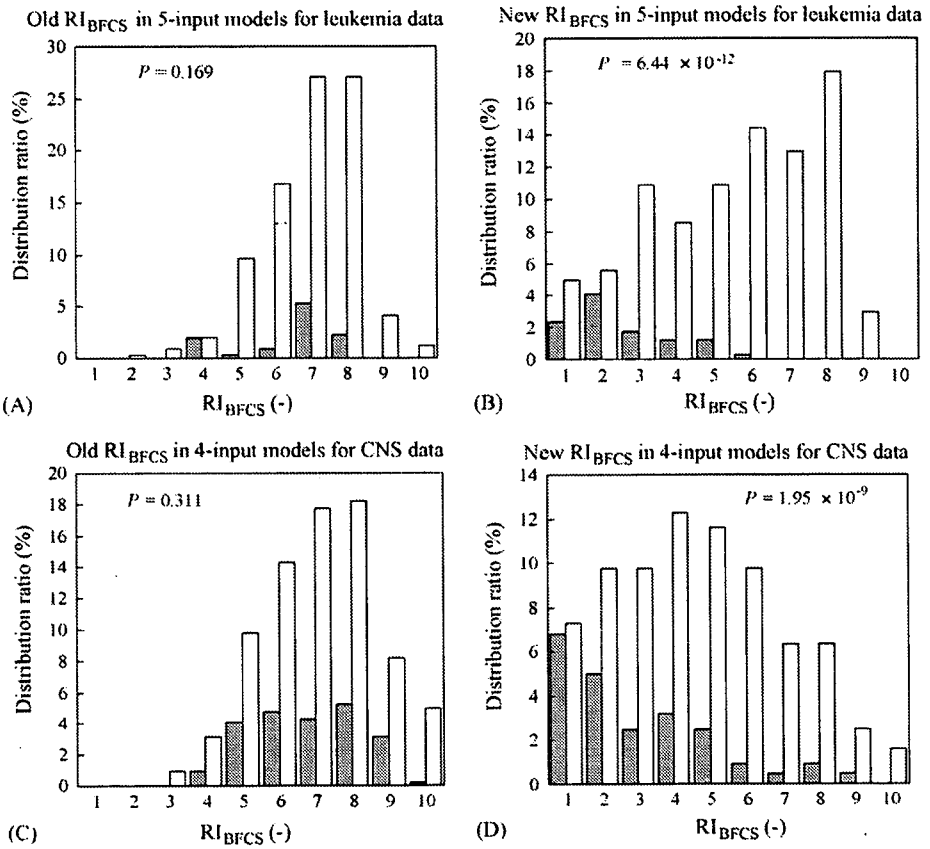

Fig. 3. Comparison of old and new RI_{BFCS}. White bars and gray bars indicate the distribution ratio of correct sample and incorrect samples, respectively. The *P*-values were calculated by Mann–Whitney test and indicate the difference in RI_{BFCS} distribution between the correct and incorrect samples.

are clearly separated ($P = 6.44 \times 10^{-12}$, 1.95×10^{-9}) for new RI_{BFCS}, as shown in Fig. 3B and D. Based on this new index, the discriminated group with over 90% prediction accuracy was separated from the others. For example, the patients who had new $RI_{BFCS} > 5$ corresponded to 48.5% of all patients for leukemia data, and an accuracy of 99.4% was achieved. And, the patients who had new $RI_{BFCS} > 5$ corresponded to 29.3% of all patients for CNS data, and a accuracy of 90.7% was achieved. This result implies new RI_{BFCS} more practical than old one. Old RI is mean distance from boundary line for each gene. BFCS is one of voting methods by assembling simple methods. Improved RI is modified by adding each signs of simple models in the BFCS model. Thus, improved RI is superior to old RI.

3.3. Comparison of selected genes with known prognostic marker genes

We investigated the presence of previously reported prognostic marker genes among the genes selected in the 10 constructed combinations of four-input PART-BFCS models. There were total of 40 genes in 10 models. Some genes were selected several times. In the case of PART-BFCS, 14 genes among 40 genes are independent, as shown in Table 4. Three genes among these 14 genes were reported to be prognostic markers for cancer: The *CCND1* gene was reported by Tan et al. [20] to be a high-risk marker gene. *CCND1* plays an important role in regulating the progress of the cell division during the G1 phase of the cell cycle. Overexpression of *CCND1* correlates with sensitivity to cisplatin [21]. The *LIF* gene was reported by Park et al. [22] to be a low-risk marker gene. *LIF* induces growth arrest and differentiation of cells. The *USP4* (*UNPH*) gene was reported by Frederick et al. [23] to be a low-risk marker gene. These observations accurately matched with low or high gene expression of the above-mentioned three marker genes, as shown in Table 4. These findings suggest that the PART-BFCS method may be used to identify new marker genes.

3.4. Comparison of genes used in PART-BFCS predictors and other predictors for CNS data

We firstly compared FNN-SWEEP and BFCS to investigate numerical character of the genes selected by PART-BFCS. Both FNN-SWEEP and BFCS are based on FNN. The one-gene predictors were constructed for each gene from second input to fourth input in the two methods. And then, average modeling accuracy of one-gene predictors for 10 combinations, was calculated (Table 5). The BFCS genes used as one-gene predictors showed clearly higher accuracy than FNN-SWEEP ones, as shown in Table 5. The average modeling accuracies of the genes from second to fourth were 83.3%, 77.3% and 79.0% for BFCS, and 72.0%, 68.7% and 65.7% for FNN-SWEEP, respectively. The PIM method was used in the FNN-SWEEP. This method is